



Strong-lensing Analysis of SPT-CL J2325–4111 and SPT-CL J0049–2440, Two Powerful Cosmic Telescopes ($R_E > 40''$) from the SPT Clusters Sample

Guillaume Mahler^{1,2,3} , Keren Sharon⁴ , Matthew Bayliss⁵ , Lindsey E. Bleem^{6,7,8} , Mark Brodwin⁹ , Benjamin Floyd¹⁰ , Raven Gassis⁵, Michael D. Gladders^{7,8} , Gourav Khullar¹¹ , Juan D. Remolina González⁴ , and Arnab Sarkar¹² 

¹ STAR Institute, Quartier Agora—Allée du six Août, 19c B-4000 Liège, Belgium

² Centre for Extragalactic Astronomy, Durham University, South Road, Durham, DH1 3LE, UK

³ Institute for Computational Cosmology, Durham University, South Road, Durham, DH1 3LE, UK

⁴ Department of Astronomy, University of Michigan, 1085 S. University Ave, Ann Arbor, MI 48109, USA

⁵ Department of Physics, University of Cincinnati, Cincinnati, OH 45221, USA

⁶ Argonne National Laboratory, High-Energy Physics Division, Argonne, IL 60439, USA

⁷ Kavli Institute for Cosmological Physics, University of Chicago, 5640 South Ellis Avenue, Chicago, IL 60637, USA

⁸ Department of Astronomy and Astrophysics, University of Chicago, 5640 South Ellis Avenue, Chicago, IL 60637, USA

⁹ Department of Physics and Astronomy, University of Missouri, 5110 Rockhill Road, Kansas City, MO 64110, USA

¹⁰ Faculty of Physics and Astronomy, University of Missouri-Kansas City, 5110 Rockhill Road, Kansas City, MO 64110, USA

¹¹ Department of Physics and Astronomy and PITT PACC, University of Pittsburgh, Pittsburgh, PA 15260, USA

¹² MIT Kavli Institute for Astrophysics and Space Research, 70 Vassar St, Cambridge, MA 02139, USA

Received 2024 July 26; revised 2024 October 15; accepted 2024 November 24; published 2025 February 3

Abstract

We report the results from a study of two massive ($M_{500c} > 6.0 \times 10^{14} M_\odot$) strong-lensing clusters selected from the South Pole Telescope cluster survey for their large Einstein radius ($R_E > 40''$), SPT-CL J2325–4111 and SPT-CL J0049–2440. Ground-based and shallow Hubble Space Telescope (HST) imaging indicated extensive strong-lensing evidence in these fields, with giant arcs spanning $18''$ and $31''$, respectively, motivating further space-based imaging follow-up. Here, we present multiband HST imaging and ground-based Magellan spectroscopy of the fields, from which we compile detailed strong-lensing models. The lens models of SPT-CL J2325–4111 and SPT-CL J0049–2440 were optimized using nine and eight secure multiply imaged systems with a final image-plane rms of $0''.63$ and $0''.73$, respectively. From the lensing analysis, we measure a projected mass density within 500 kpc of $M(<500 \text{ kpc}) = (7.30 \pm 0.07) \times 10^{14} M_\odot$ and $M(<500 \text{ kpc}) = 7.12^{+0.16}_{-0.19} \times 10^{14} M_\odot$ for these two clusters, and subhalo mass ratios of 0.12 ± 0.01 and $0.21^{+0.07}_{-0.05}$, respectively. Both clusters produce a large area with high magnification ($\mu \geq 3$) for a source at $z = 9$, $\mathcal{A}_{|\mu| \geq 3}^{\text{lens}} = 4.93^{+0.03}_{-0.04} \text{ arcmin}^2$ and $\mathcal{A}_{|\mu| \geq 3}^{\text{lens}} = 3.64^{+0.14}_{-0.10} \text{ arcmin}^2$, respectively, placing them in the top tier of strong-lensing clusters. We conclude that these clusters are spectacular sightlines for further observations that will reduce the systematic uncertainties due to cosmic variance. This paper provides the community with two additional well-calibrated cosmic telescopes, as strong as the Frontier Fields and suitable for studies of the highly magnified background Universe.

Unified Astronomy Thesaurus concepts: Strong gravitational lensing (1643); Galaxy clusters (584); Galactic and extragalactic astronomy (563); Dark matter (353); High-redshift galaxies (734)

Materials only available in the online version of record: machine-readable table

1. Introduction

Clusters of galaxies are located at the nodes of the cosmic web and represent the largest structures of dark matter. Their mass distribution presents a remarkable self-similarity in the outskirts (M. McDonald et al. 2017). However, the densest region located at the core of the structure deviates from this scale-free distribution. This region is prone to ongoing merging activity, where both luminous and dark matter coevolve. While luminous matter is commonly observed, dark matter remain elusive and is only probed indirectly. Fortunately, the densest regions of cluster cores produce strong gravitational lensing, offering constraining power to map the underlying matter distribution regardless of its nature and provide a magnified view of the distant Universe.

Past studies have used strong-lensing clusters to study a large breadth of topics, often even in one sightline. Frequently addressed questions focus on: the detailed mapping of the underlying matter distribution in the cluster, estimating both visible and dark contributions (e.g., M. Jauzac et al. 2014; L. J. Furtak et al. 2023); tests of cold dark matter (CDM) alternative candidates (D. Harvey et al. 2017; P. Natarajan et al. 2017; A. Robertson et al. 2019; E. L. Sirks et al. 2022); comparisons of occurrences of galaxy–galaxy lenses in the dense environments of clusters to simulations (M. Meneghetti et al. 2020; A. Robertson 2021); detection of filamentary structure, connecting cluster halos to the cosmic web (e.g., M. Jauzac et al. 2012; S.-I. Tam et al. 2022); constraints on the galaxy halo/subhalo mass ratio (G. Mahler et al. 2019) and subhalo mass function (e.g., P. Natarajan et al. 2017; E. L. Sirks et al. 2022); constraining the clumpiness of lensing mass, producing microlensing from stars and primordial black holes (e.g., J. M. Diego et al. 2018; P. L. Kelly et al. 2018; G. Mahler et al. 2023b); measuring spatially-resolved

properties of giant arcs, such as winds (T. C. Fischer et al. 2019), sizes of star-forming clumps (T. L. Johnson et al. 2017; A. Claeysens et al. 2023), metallicity gradients and kinematics (V. Patrício et al. 2018), and leaking ionizing photon radiation (Rivera-Thorsen et al. 2019) at a resolution of tens of parsecs at $z > 1$; using caustic crossing events to probe stars at the dawn of the Universe (e.g., B. Welch et al. 2022; T. Y.-Y. Hsiao et al. 2023; A. Adamo et al. 2024); detecting magnified high-redshift galaxies, probing the intrinsically fainter galaxies more representative of early populations (H. Atek et al. 2024) and offering constraints on the faint end of the high- z luminosity function (H. Atek et al. 2015; R. J. Bouwens et al. 2017; R. C. Livermore et al. 2017; G. de La Vieuville et al. 2019); constraining cosmological parameters such as the dark energy equation-of-state parameter (w) and Ω_M (e.g., E. Jullo et al. 2010; A. Acebron et al. 2017), and time-delay measurements of H_0 (e.g., C. Grillo et al. 2018; K. Napier et al. 2023).

Owing to their diverse core properties (M. McDonald et al. 2017), clusters with the same total mass may not exhibit similar strong-lensing cross sections. To identify strong-lensing lines of sight requires selection-based properties beyond their total mass. Two main methods of discovery are employed to find lines of sight of lensing clusters: lensing-selected and non-lensing-selected. Lensing-selected surveys have traditionally searched for substantial lensing evidence, typically in the form of highly magnified giant arcs by inspection of large data sets of shallow ground-based data. Utilizing the data and catalogs of the Sloan Digital Sky Survey resulted in numerous lenses (e.g., M. B. Bayliss et al. 2011a, 2011b; D. P. Stark et al. 2013; H. Dahle et al. 2015; T. L. Johnson et al. 2017; K. Sharon et al. 2020), mainly at low arc and lens redshifts. More recently, imaging from the Dark Energy Survey yielded strong-lensing samples based on visual inspection (e.g., H. T. Diehl et al. 2017; G. Khullar et al. 2021) or machine-assisted identification (e.g., X. Huang et al. 2021).

Non-lensing-based approaches commonly rely on deep or high-resolution optical imaging follow-up of cluster samples that were selected as likely lenses based on other criteria, usually high total mass as indicated from X-ray, submillimeter, or optical mass proxies. Examples of such surveys include the Hubble Space Telescope (HST) follow-up of the Massive Cluster Survey (MACS; H. Ebeling et al. 2001), the optical ground-based and HST follow-up of the South Pole Telescope (SPT) cluster sample (L. E. Bleem et al. 2015, 2020), the Local Cluster Substructure Survey (LoCuSS; G. P. Smith et al. 2005) follow-up of X-ray-selected clusters, HST follow-up of submillimeter-selected lens candidates (dusty GEM; R. Cañameras et al. 2015), and spectroscopic follow-up of X-ray-selected clusters with Very Large Telescope/MUSE (e.g., KALEIDOSCOPE cluster survey, P.ID: 0102.A-0718 (A), PI: A. Edge; N. R. Patel et al. 2024). Several treasury programs with HST employed a hybrid selection approach where lensing evidence from shallower or low-resolution imaging was combined with total mass criteria to increase the sample, e.g., CLASH (25 clusters, M. Postman et al. 2012) and RELICS (41 clusters, D. Coe et al. 2019).

To fully benefit from the lines of sight of strong gravitational lenses requires space-based observations, such as with HST or JWST, and relatively shallow HST follow-up of the aforementioned samples resulted in numerous discoveries as listed at the beginning of the introduction. However, the high investment of space-based telescope time is reserved for a few, extraordinary lenses, carefully picked as the best lenses coming out of the

previous surveys. Such are the Frontier Fields (J. M. Lotz et al. 2017), for which the original program used 840 HST orbits to observe six strong-lensing clusters. More recently, studies of cluster-lensed galaxies using JWST (e.g., TEMPLATES, J. R. Rigby et al. 2025; UNCOVER, R. Bezanson et al. 2024; PEARLS, R. A. Windhorst et al. 2023; SMACSJ0723, G. Mahler et al. 2023a; G. B. Caminha et al. 2022; M. Golubchik et al. 2022; SPT0615, A. Adamo et al. 2024; WHL0137, B. Welch et al. 2022) have pushed the limits of redshift, luminosity, and resolution.

While tremendous discoveries were enabled even in single well-studied lines of sight (e.g., UNCOVER; R. Bezanson et al. 2024), both the HST and JWST analyses caution that cosmic variance might play an important role in our ability to infer the properties of high-redshift populations of galaxies. B. Salmon et al. (2020) identified 322 new candidates at $z > 6$ behind the 41 clusters uniformly observed by HST as part of RELICS, reporting a large field-to-field variance, where in some fields no galaxy candidates beyond $z > 5.5$ were found (G. Mahler et al. 2019). A recent JWST analysis (I. Chemerynska et al. 2024) reported a potential overabundance of UV galaxies behind the lensing cluster A2744. Identifying more clusters that are on par with the lensing power of the Frontier Fields clusters will open up an important discovery space.

This paper presents two new exquisite well-calibrated strong-lensing sightlines with obvious untapped discovery potential coming at the end of a dedicated search based on SPT optical follow-up using the PISCO imager and HST/SNAP follow-up. These targets, SPT-CL J2325–4111 and SPT-CL J0049–2440, are two of the most promising strong-lensing clusters from the SPT cluster sample.

The SPT cluster sample is based on the detection and calibration of the Sunyaev–Zel’dovich (SZ) effect observed in the cosmic microwave background radiation (L. E. Bleem et al. 2015, 2020 and references therein). The entire cluster sample was followed up with multiband imaging using Magellan/PISCO (B. Stalder et al. 2014; L. E. Bleem et al. 2020), facilitating the identification of strong-lensing candidates, among other cluster science (e.g., T. Somboonpanyakul et al. 2021) and extensive spectroscopic campaigns using Magellan and Gemini (M. B. Bayliss et al. 2016). Some clusters were the target of HST programs mainly for weak-lensing calibration (e.g., T. Schrabback et al. 2021) and HST/SNAP programs provided shallow high-resolution imaging (M. D. Gladders et al. 2019).

SPT-CL J2325–4111 was reported on by L. E. Bleem et al. (2015, 2020) as a $\xi = 12.5$ significance SZ detection,¹³ with ground-based spectroscopic redshift of $z = 0.358$ (J. Ruel et al. 2014). S. Bocquet et al. (2019) report $M_{500c} = 6.70^{+0.95}_{-1.17} \times 10^{14} h_{70}^{-1} M_{\odot}$ from the weak-lensing calibrated SZ signal. It was flagged as a strong-lensing cluster in Table 4 of L. E. Bleem et al. (2015).

SPT-CL J0049–2440 was reported on by L. E. Bleem et al. (2020) from an analysis of the SPTPol Extended Cluster Survey as a $\xi = 7.44$ significance SZ detection, with ground-based spectroscopic redshift of $z = 0.527$ (R. de Propris et al. 1999). L. E. Bleem et al. (2020) report $M_{500c} = 6.59^{+0.86}_{-0.98} \times 10^{14} h_{70}^{-1} M_{\odot}$ from the weak-lensing calibrated SZ signal. The same paper

¹³ The SZ significance ξ for SPT clusters is defined as the detection signal-to-noise ratio, maximized over the 12 filters that SPT uses for cluster identification, with scales ranging from 0.25 to 3.0; see K. Vanderlinde et al. (2010).

Table 1
List of Lensing Constraints

ID	R.A. J2000	Decl. J2000	z_{spec} or z_{model}	Dist. (arcsec)	μ	Notes
SPT-CL J2325–4111 Source 1			1.5790			GMOS; single giant arc; SL by nearby galaxy
1.1.1	351.296820	−41.187381		0.19	$8.2^{+0.1}_{-0.3}$	Clump 1
1.2.1	351.295943	−41.187662		0.11	$4.4^{+0.4}_{-0.7}$	
1.1.2	351.296463	−41.187529		0.16	$24.5^{+3.1}_{-2.3}$	Clump 2
1.2.2	351.296232	−41.187615		0.09	$12.7^{+3.0}_{-2.0}$	
SPT-CL J2325–4111 Source 2			2.4253			FIRE spec of 2.3, from O III, H β , H α ; 2019-12-04
2.1.1	351.301880	−41.192335		0.51	$2.5^{+0.2}_{-0.2}$	Clump 1
2.2.1	351.285884	−41.202655		0.31	$5.0^{+0.1}_{-0.3}$	
2.3.1	351.303568	−41.209014		0.44	$8.4^{+0.3}_{-0.3}$	
2.4.1	351.312449	−41.197529		0.28	$25.1^{+2.7}_{-1.2}$	
2.5.1	351.299833	−41.202644		0.28	$1.4^{+0.2}_{-0.1}$	
2.1.2	351.302765	−41.192171		1.31	$7.7^{+0.7}_{-0.1}$	Clump 2
2.2.2	351.285764	−41.202283		0.78	$7.6^{+0.7}_{-0.3}$	
2.3.2	351.304206	−41.208597		0.60	$10.2^{+0.5}_{-0.4}$	
2.4.2	351.312034	−41.197256		0.30	$13.1^{+0.3}_{-0.7}$	
SPT-CL J2325–4111 Source 3			3.8180			FIRE spec of 3.1, both O III lines in the <i>K</i> band; 2019-12-05
3.1	351.306626	−41.189283		0.21	$42.1^{+7.2}_{-2.9}$	
3.2	351.301163	−41.188301		0.36	$5.8^{+0.6}_{-0.6}$	
3.3	351.285310	−41.196210		0.59	$4.7^{+0.2}_{-0.1}$	
3.4	351.301139	−41.207554		0.85	$3.0^{+0.1}_{-0.2}$	
SPT-CL J2325–4111 Source 4			1.3180			FIRE spec of 4.3, H α ; 2019-12-05
4.1	351.291829	−41.206459		1.03	$7.8^{+0.2}_{-0.2}$	
4.2	351.297771	−41.209536		0.56	$3.5^{+0.2}_{-0.3}$	
4.3	351.311327	−41.203079		1.19	$8.6^{+0.3}_{-0.2}$	
4.4	351.298830	−41.197679		1.03	$6.7^{+0.2}_{-0.8}$	Radial arc
SPT-CL J2325–4111 Source 5			1.29 ± 0.01			
5.1	351.293221	−41.208914		0.73	$9.7^{+0.3}_{-0.4}$	
5.2	351.298529	−41.210439		0.27	$8.9^{+0.4}_{-0.6}$	
5.3	351.306435	−41.208372		0.82	$13.0^{+0.4}_{-0.7}$	
SPT-CL J2325–4111 Source 6			7.02 ± 0.20			
6.1	351.313070	−41.189842		1.64	$4.9^{+0.2}_{-0.2}$	
6.2c	351.292582	−41.189019		...	$14.4^{+1.1}_{-1.1}$	
6.3	351.288051	−41.192324		2.80	$12.0^{+0.4}_{-0.5}$	
6.4	351.299692	−41.207262		0.84	$2.1^{+0.1}_{-0.1}$	
SPT-CL J2325–4111 Source 7			...			Candidate system
7.1c	351.293554	−41.194939				
7.2c	351.292862	−41.195442				
SPT-CL J2325–4111 Source 8			3.00 ± 0.16			
8.1	351.302596	−41.198158		0.42	$7.7^{+0.6}_{-0.7}$	Radial arc
8.2	351.301964	−41.198866		0.48	$22.5^{+7.6}_{-4.4}$	Radial arc
8.3	351.305018	−41.194379		0.04	$4.0^{+0.4}_{-1.0}$	
SPT-CL J2325–4111 Source 9			1.21 ± 0.01			
9.1	351.305663	−41.207017		0.38	$18.5^{+1.0}_{-0.7}$	
9.2	351.301553	−41.208875		0.49	$13.4^{+0.8}_{-0.5}$	
9.3	351.290113	−41.205325		0.42	$4.9^{+0.1}_{-0.2}$	
SPT-CL J0049–2440 Source 1			3.0220			FIRE spec of 1.2; O III
1.1.1	12.306837	−24.678576	3.0220	0.32	$6.4^{+0.8}_{-0.4}$	
1.2.1	12.304789	−24.673793		0.31	$6.8^{+1.1}_{-0.8}$	
1.3.1c	12.293434	−24.669124		...	$8.9^{+1.3}_{-0.6}$	Spectroscopy attempted, not confirmed
1.4.1	12.290510	−24.685268		0.30	$2.2^{+0.5}_{-0.2}$	
1.1.2	12.306927	−24.679502		0.47	$5.7^{+0.9}_{-0.2}$	Clump near arc 1, assumed to be at the same z
1.3.2c	12.293478	−24.669244		...	$9.8^{+1.5}_{-0.7}$	
1.4.2	12.290435	−24.685274		0.18	$2.3^{+0.5}_{-0.3}$	
SPT-CL J0049–2440 Source 2			1.52 ± 0.10			
2.1	12.296863	−24.668930		0.15	$19.9^{+4.5}_{-1.3}$	
2.2	12.297035	−24.668981		0.14	$4.3^{+1.2}_{-0.7}$	
2.3	12.297701	−24.669017		0.22	$5.0^{+0.6}_{-0.4}$	
SPT-CL J0049–2440 Source 3			3.62 ± 0.31			

Table 1
(Continued)

ID	R.A. J2000	Decl. J2000	z_{spec} or z_{model}	Dist. (arcsec)	μ	Notes
3.1	12.302022	-24.681788		0.19	$5.5^{+0.7}_{-0.6}$	
3.3	12.281064	-24.672098		0.23	$2.5^{+0.2}_{-0.2}$	
3.4	12.297052	-24.680913		0.12	$3.7^{+0.6}_{-0.4}$	
SPT-CL J0049-2440 Source 4			3.03 ± 0.16			
4.1	12.284454	-24.681115		0.05	$11.7^{+0.8}_{-0.9}$	
4.2c	12.285342	-24.683749		...	$13.9^{+2.9}_{-2.9}$	
4.3	12.303653	-24.689925		0.10	$3.9^{+0.2}_{-0.2}$	
SPT-CL J0049-2440 Source 5			1.37 ± 0.03			
5.1	12.291012	-24.680759		2.43	$12.8^{+0.9}_{-0.9}$	Radial arc
5.2	12.291352	-24.680671		1.98	$12.9^{+1.0}_{-0.8}$	Radial arc
5.3	12.293889	-24.678894		0.40	$9.1^{+0.8}_{-0.3}$	
5.4	12.303297	-24.684562		1.42	$3.2^{+0.2}_{-0.3}$	
SPT-CL J0049-2440 Source 6			2.368			FIRE spec of both 6.1 and 6.2; O III
6.1	12.298507	-24.681234	2.368	0.11	71^{+70}_{-7}	Radial arc
6.2	12.298314	-24.681211	2.368	0.20	860^{+90}_{-12}	Radial arc
SPT-CL J0049-2440 Source 7			2.30 ± 0.10			
7.1	12.296999	-24.680492		0.02	$4.3^{+0.7a}_{-0.4a}$	
7.2	12.300114	-24.680802		0.62	$4.9^{+1.0}_{-0.4}$	
7.3	12.301315	-24.680923		0.54	$3.5^{+0.5}_{-0.3}$	
7.4	12.282750	-24.673044		0.01	$2.9^{+0.3}_{-0.1}$	
SPT-CL J0049-2440 Source 8			4.96 ± 0.61			
8.1	12.298777	-24.688750		0.10	13^{+2}_{-1}	
8.2	12.295079	-24.689882		0.08	56^{+18}_{-11}	

Note. The IDs, positions, and redshifts of lensed galaxies that were used as constraints in this work. Where possible, individual emission knots in each image are identified and used as lensing constraints. The IDs of images of lensed galaxies are labeled as A.B(C) where A is the number indicating the source ID (or system name), B is the number indicating the ID of the lensed image within the family of multiple images, and C is a number indicating the ID of the emission knot within the image if we used more than one substructure of the images as constraints. Lower-case *c* indicates a candidate arc that was not used to constrain the model. Dist, often called individual rms, is the distance in the image plane between the observed and model-predicted locations of an image. The model-predicted location is calculated as the lensed coordinates of the geometric mean of source positions of all the multiple images of a given source.

highlights this cluster as a prominent strong lens, first reported on by R. de Propris et al. (1999).

In this paper, we used multiband HST imaging and ground-based spectroscopy to identify lensing evidence, compute lens models, and calculate lens properties such as mass distribution, magnification, and lensing strength, showing that these clusters are excellent new strong lenses. This paper is organized as follows. We present the data used in this work in Section 2 and the lens modeling analysis in Section 3. In Section 4 we discuss the mass distribution and lensing power of those clusters, and highlight prominent lensed sources. We conclude in Section 5. We also report in Appendix B the HST imaging and spectroscopic follow-up of a third cluster from the same program, SPT-CL J0512-3848, which did not pan out as a similarly powerful cosmic telescope.

We assume flat Λ CDM cosmology with $\Omega_{\Lambda} = 0.7$, $\Omega_m = 0.3$, and $H_0 = 70 \text{ km s}^{-1} \text{ Mpc}^{-1}$. Magnitudes are reported in the AB system (J. B. Oke 1974).

2. Data and Lensing Evidence

2.1. Hubble Space Telescope

The fields studied in this paper were observed by HST as part of Cycle 27 GO-15937 (PI: G. Mahler). Each cluster was observed

with four filters, using three orbits of HST: one orbit with the ACS/F606W filter, one orbit with the ACS/F814W filter, and one orbit with WFC3-IR split between two filters, F105W and F140W. We obtained four subexposures per filter with small box subpixel dithers to reconstruct the point-spread function and to cover chip gaps and artifacts such as the ‘‘IR Blobs’’ and ‘‘Death Star’’ (WFC3 Data Handbook; A. Rajan 2010). For the WFC3-IR observations we used a sampling interval parameter SPARS25.

Observations of SPT-CL J2325-4111 took place on 2019 October 22 (WFC3) and 2019 October 25 (ACS). The second visit was affected by a guide-star reacquisition error, leading to a lost exposure in the F814W band, and was rescheduled by HOPR 91651 to 2019 December 10. The resulting imaging data have 1212 s in WFC3/F105W, 1312 s in WFC3/F140W, 2204 s in ACS/F606W, and 3477 s in ACS/F814W. The failed F814W subexposure was not used. Observations of SPT-CL J0049-2440 took place on 2019 October 23 (WFC3) and 2019 October 31 (ACS), and consist of 1212 s each in WFC3-IR/F105W and F140W, 2124 s in ACS/F606W, and 2184 s in ACS/F814W.

Data reduction was done similarly to K. Sharon et al. (2020). We combined all the usable subexposures of each filter with the AstroDrizzle package (S. Gonzaga et al. 2012) with a pixel scale of $0''.03 \text{ pixel}^{-1}$, and drop size of 1.0 for the ACS images and 0.8 for WFC3. Observations that were executed over

multiple visits were aligned to a common world coordinate system (WCS) using `tweakreg`, and the WCS solutions were applied back to the individual subexposures with `tweakback`. Finally, we drizzled all the images of each field onto the same pixel frame using the same parameters as above. The clusters are presented in Figures 1 and 2.

2.2. Lensing Evidence

Multiple images (arcs) of background galaxies are used as strong-lensing evidence to constrain the lens model of each cluster. We identified multiple images of each background source through visual inspection of the HST imaging, based on color and morphology of the images. We have obtained spectroscopic confirmation of a subset of those (see Section 2.3 below). Figures 1 and 2 show the identified multiple images in each field overplotted on the HST data (see also Figure 9 in Appendix C for zoom-ins of all multiply imaged systems identified). The multiple images of each source are labeled and color-coded by source ID. The

coordinates, spectroscopic redshift information, and other notes specific to each system are listed in Table 1. In some of these sources we further identified emission clumps or other substructure that could be matched between images and used as additional constraints in the lens models. The IDs of images of lensed galaxies are labeled as A.B(C) where A indicates the source ID (or system name), B identifies the lensed image within the family of multiple images, and C is the ID of the emission knot within the image if we used more than one substructure of the images as a constraint. For example, ID 1.3.2 would identify the third multiple image of knot #2 in Source 1.

In SPT-CL J2325–4111 we identified a total of nine secure strongly lensed sources with multiple images. Of these, four strongly lensed sources are spectroscopically confirmed. In the field of SPT-CL J0049–2440 we identified a total of eight secure systems, with spectroscopic redshifts for two. Other arclike features that were not used in this analysis can be seen in the HST images. We further discuss the lensing evidence in Section 3.2.

Table 2
Lens Model Results and Best-fit Parameters

Model Name	Component	α^a	δ^a	e^b	θ^c	σ_0^d	r_{cut}	r_{core}
SPT-CL J2325–4111	Halo 1 (cluster)	$7.34^{+0.28}_{-0.36}$	$11.99^{+0.94}_{-1.01}$	$0.29^{+0.01}_{-0.01}$	$73.7^{+0.6}_{-0.8}$	$1332.2^{+14.2}_{-20.1}$	[1500]	$39.9^{+0.1}_{-1.7}$
rms = 0."63; $k = 30$	Halo 2 (galaxy)	[0.0]	[0.0]	[0.29]	[–83.04]	$619.1^{+25.8}_{-20.0}$	$21.8^{+4.5}_{-4.4}$	$4.1^{+0.5}_{-0.3}$
$\chi^2/\nu = 9.0$; dof = 16	Halo 3 (galaxy)	[3.40]	[16.21]	[0.31]	[77.46]	$407.1^{+6.0}_{-17.2}$	$86.0^{+17.3}_{-10.8}$	$2.0^{+0.1}_{-0.4}$
$\log(\mathcal{L}) = -54$	Halo 4 (galaxy)	[–9.04]	[47.91]	[0.16]	[–43.21]	$134.8^{+15.6}_{-14.5}$	$9.2^{+10.2}_{-13.8}$	$1.4^{+0.2}_{-1.2}$
$\log(\mathcal{E}) = -123$	Halo 5 (galaxy)	[14.95]	[30.10]	[0.13]	[22.48]	$287.4^{+8.3}_{-7.7}$	$54.1^{+6.7}_{-8.3}$	$1.2^{+0.2}_{-0.3}$
BIC = 233 AICc = 221	Halo 6 (galaxy)	[24.61]	[21.27]	[0.27]	[–18.06]	$100.2^{+25.5}_{-0.9}$	$3.4^{+4.5}_{-0.2}$	$0.9^{+1.1}_{-0.3}$
	Halo 7 (galaxy)	[35.78]	[18.15]	[0.12]	[25.57]	$19.7^{+14.9}_{-6.0}$	$37.8^{+35.9}_{-0.8}$	$2.0^{+0.4}_{-0.7}$
	L^* Galaxy	$207.6^{+12.7}_{-6.1}$	$56.8^{+13.0}_{-12.4}$...
SPT-CL J0049–2440	Halo 1 (cluster)	$-7.95^{+0.87}_{-2.34}$	$-8.28^{+0.33}_{-2.22}$	$0.4^{+0.02}_{-0.09}$	$136.5^{+3.7}_{-1.5}$	$1145.5^{+49.3}_{-28.9}$	[1500]	$16.9^{+3.2}_{-1.8}$
rms = 0."73; $k = 24$	Halo 2 (galaxy)	$1.42^{+0.41}_{-0.53}$	$-1.89^{+0.39}_{-0.5}$	$0.37^{+0.03}_{-0.03}$	$76.1^{+23.3}_{-11.3}$	$494.7^{+155.0}_{-29.0}$	$117.7^{+16.3}_{-28.8}$	$3.7^{+1.7}_{-0.6}$
$\chi^2/\nu = 19.0$; dof = 8	Halo 3 (galaxy)	[25.08]	[10.83]	[0.42]	[–51.14]	$267.0^{+13.5}_{-15.2}$	$10.7^{+0.7}_{-0.8}$	$0.8^{+0.4}_{-0.2}$
$\log(\mathcal{L}) = -61$	L^* Galaxy	$273.5^{+4.9}_{-19.1}$	$175.6^{+20.5}_{-28.3}$...
$\log(\mathcal{E}) = -323$
BIC = 215 AICc = 218

Notes.

^a α and δ are the positions measured in arcseconds relative to the reference coordinate point for SPT-CL J2325–4111 (R.A. = 351.298863, decl. = –41.203566) and SPT-CL J0049–2440 (R.A. = 12.295750, decl. = –24.678583).

^b Ellipticity (e) is defined as $(a^2 - b^2)/(a^2 + b^2)$, where a and b are the semimajor and semiminor axes of the ellipse.

^c θ is measured north of east.

^d σ_0 is the normalization parameter and represents a fiducial central velocity dispersion as defined in the dPIE parameterization. Statistical uncertainties were inferred from the MCMC optimization and correspond to a 68% confidence interval. Parameters in square brackets were not optimized. The position and the ellipticities of the mass clumps associated with cluster galaxies were kept fixed according to their light distribution, and the other parameters were determined through scaling relations (see text).

^e Fit results for each model are given in the left column. rms is the scatter in the image plane; k is the number of free parameters; dof stands for the number of degrees of freedom; BIC is the Bayesian information criterion and AICc is the corrected Akaike information criterion.

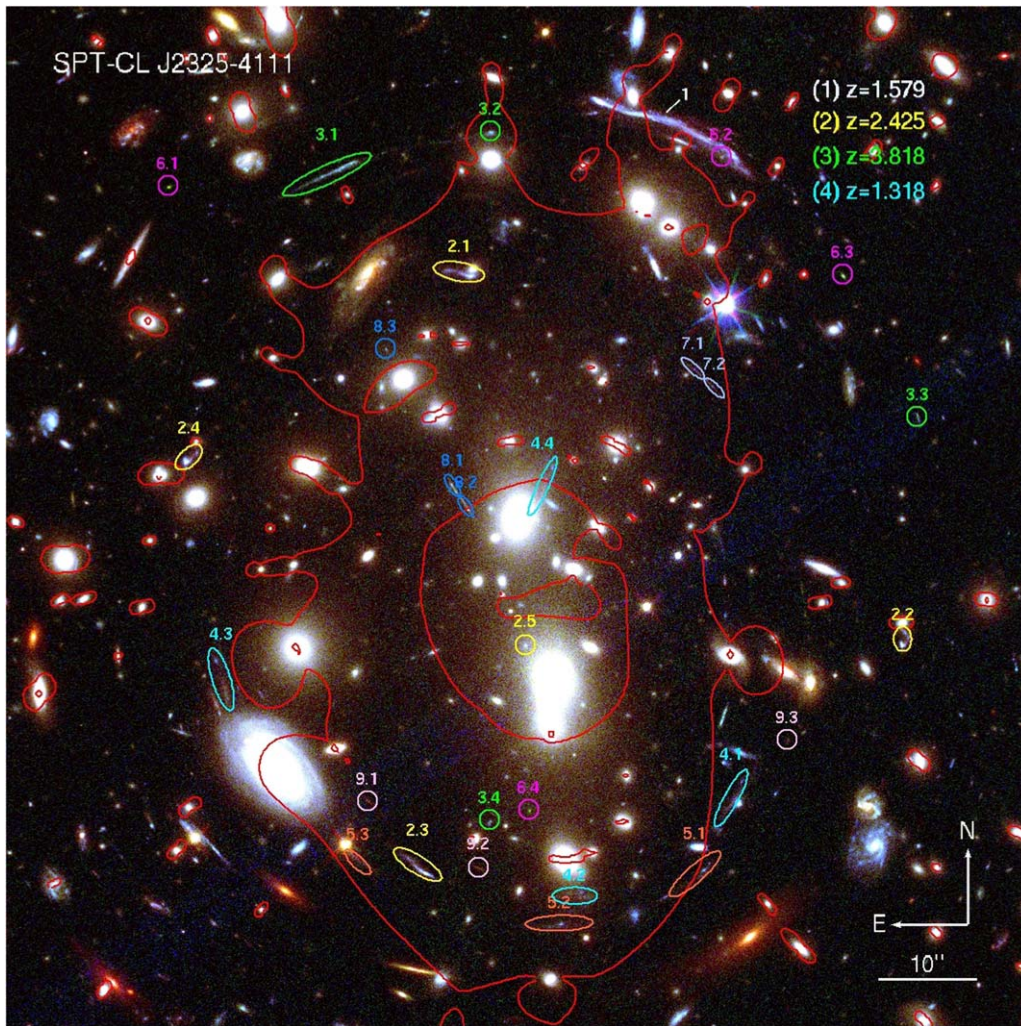


Figure 1. Composite color images of the field of SPT-CL J2325–4111, from HST imaging in WFC3-IR/F140W (red), ACS/F814W (green), and ACS/F606W (blue). Multiple images of lensed features are labeled and color-coded by the source ID. The coordinates, redshifts (where available), and references of these strong-lensing systems are presented in Table 1. The critical curve for a source plane at $z = 2$ is shown in solid red. North is up and east is to the left.

2.3. Spectroscopy

Spectroscopic observations of SPT-CL J2325–4111 and SPT-CL J0049–2440 were obtained as part of larger campaigns to follow up SPT-selected clusters of galaxies. We collected all the available spectroscopy for these two clusters for the primary purpose of measuring spectroscopic redshifts of candidate lensed sources and cluster-member galaxies. These observations used the Magellan 6.5 m telescopes at Las Campanas Observatory, with the Inamori-Magellan Areal Camera and Spectrograph (IMACS; A. Dressler et al. 2011) on Magellan I-Baade, the upgraded Low Dispersion Survey Spectrograph (LDSS3-C) on Magellan II-Clay, and the Folded port InfraRed Echellette (FIRE; R. A. Simcoe et al. 2013) spectrograph on Magellan I-Baade. We describe the observations and data reduction of Magellan LDSS3, IMACS, and FIRE in the following subsections. Spectroscopic results for specific objects in the following subsection refer to the object IDs in Figure 1, Figure 2, and Table 1. The compilation of spectroscopic catalogs for these fields is described in Section 2.4.

2.3.1. Magellan LDSS3 and IMACS MOS Spectroscopy

We obtained spectroscopy of SPT-CL J2325–4111 and SPT-CL J0049–2440 with custom-designed multiobject slit (MOS)

masks (J. D. Remolina González 2021). Spectroscopic observations that took place before the HST data were in hand used Magellan/PISCO imaging to guide the mask design (see L. E. Bleem et al. 2020, for description of the PISCO data).

SPT-CL J2325–4111 was observed with LDSS3 on 2016 June 7, with two MOS masks, each observed for 4×25 minutes, in clear conditions and seeing of $1''.0$. Slits were placed on candidate lensed features as identified from ground-based imaging, including 2.1, 2.3, 3.1, 4.1, 4.3, and on cluster-member galaxies selected by color. SPT-CL J0049–2440 was observed with LDSS3 on 2017 December 20, with one MOS mask, 2×20 minutes exposure, in clear weather and $0''.8$ seeing. Slits were placed on candidate lensing features, including 1.2, 5.1/5.2, 6.1/6.2, and 4.3, and cluster-member galaxies.

SPT-CL J2325–4111 was observed with IMACS on 2015 May 27, in clear weather and seeing of $0''.7 - 0''.75$. We observed one MOS mask in three subexposures, for a total of 6600 s, using the `IMACS_grism_200` disperser. Only 10 out of the 108 slits were within the HST field of view, targeting arclike features as identified from ground-based data, including the giant arc of source 1 for which a spectroscopic redshift of $z = 1.5790$ was previously observed with Gemini/GMOS

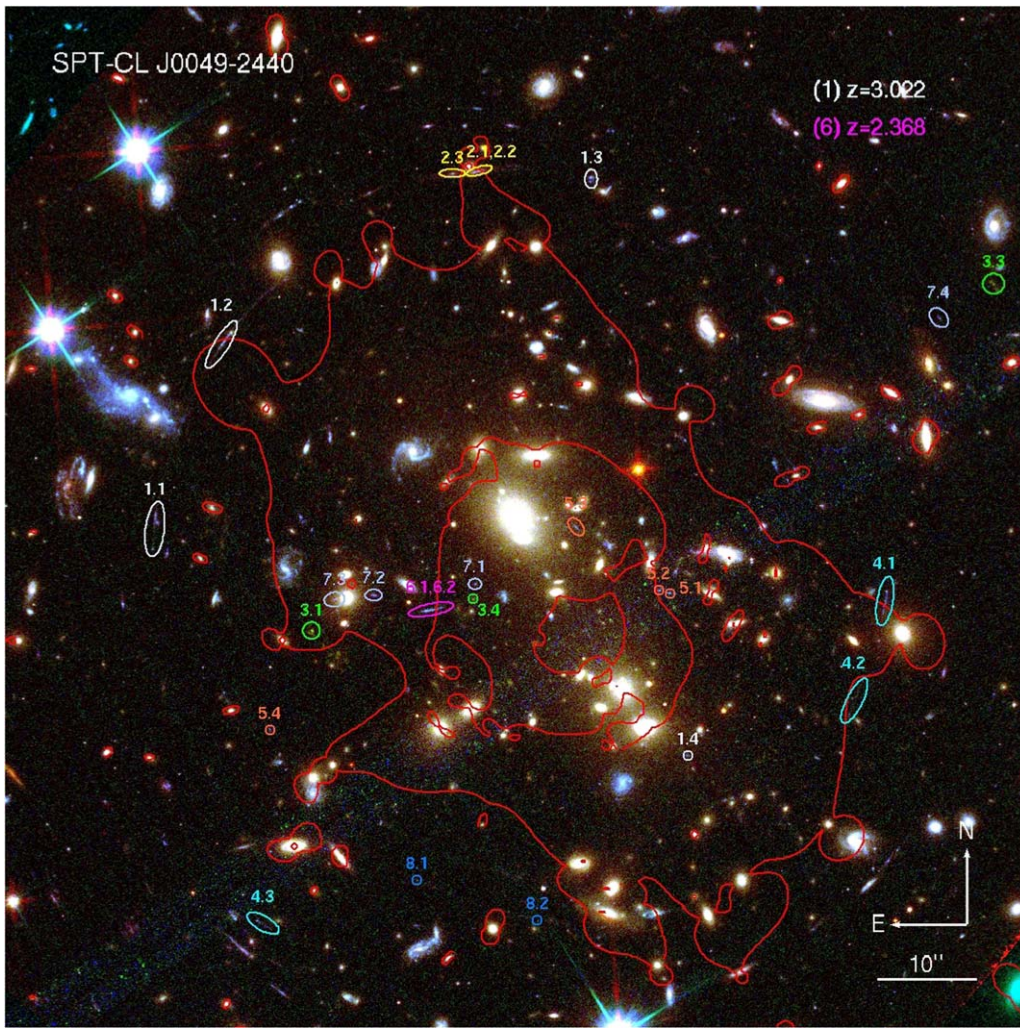


Figure 2. Composite color images of the field of SPT-CL J0049–2440, from HST imaging in WFC3-IR/F140W (red), ACS/F814W (green), and ACS/F606W (blue). Multiple images of lensed features are labeled and color-coded by the source ID. The coordinates, redshifts (where available), and references of these strong-lensing systems are presented in Table 1. The critical curve for a source plane at $z = 2$ is shown in solid red. North is up and east is to the left.

(M. B. Bayliss et al. 2016). The remaining slits in the large field of view of IMACS were placed primarily on cluster-member galaxies, selected by color from ground-based photometry.

We reduced the LDSS3 and IMACS spectra using the Carnegie Observatories System for Multi-Object Spectroscopy (COSMOS; A. Dressler et al. 2011; A. Oemler et al. 2017).¹⁴ The debiased raw data were flat-fielded using flat-field images that were taken immediately before or after each science frame. For wavelength calibration, we used HeNeAr comparison arc frames, also taken immediately before or after each science observation. Subexposures of the same mask were coadded, and the off-source area within the same slit was used to subtract the sky. The 1D spectrum of each targeted object was extracted using custom Python routines following standard methods.

While yielding ample redshifts for cluster-member galaxies and foreground objects, both LDSS3 and IMACS had limited success in securing spectroscopic redshifts of lensed galaxies. This was in part because these observations took place prior to our HST program and many arcs were not identified at the time, and in part due to the wavelength coverage of these instruments.

2.3.2. Magellan FIRE Spectroscopy of Arc Candidates

SPT-CL J2325–4111 and SPT-CL J0049–2440 were spectroscopically observed with the FIRE spectrograph on 2019 December 4 and 5, in good conditions, and seeing ranging between $0''.55$ and $1''.0$. Data reduction used standard IRAF techniques, and the redshifts were measured from lines identified primarily in the 2D spectra.

In the field of SPT-CL J2325–4111, we targeted arcs 2.3, 7.1, 8.1, and 3.1 on the first night and arcs 2.2, 4.3, 3.1, and c1 (a blue arclike feature north of 4.1) on the second night. Each target was observed with a $1''.0$ slit for 2×602 s unless otherwise specified, executing a small A/B dither along the slit between exposures.

We measured secure redshifts for three sources with FIRE. Source 2 is at $z = 2.4253 \pm 0.0007$, based on bright [O III], $H\alpha$, and $H\beta$ lines in emission in the spectrum of arc 2.3. We identified the same lines in the spectrum of arc 2.2, an image of the same source, obtained on the second night. The spectrum of arc 3.1 on night 1 was inconclusive; A deeper observation of 2×1205 s was obtained for arc 3.1 on the second night, resulting in a secure redshift of 3.8180 ± 0.0007 from two O III $\lambda\lambda 4959, 5007$ lines.

We identified one line in the spectrum of arc 4.3, which can be interpreted as either [O III] $\lambda 5007$ at $z = 2.037$ or $H\alpha$ at

¹⁴ <https://code.obs.carnegiescience.edu/cosmos>

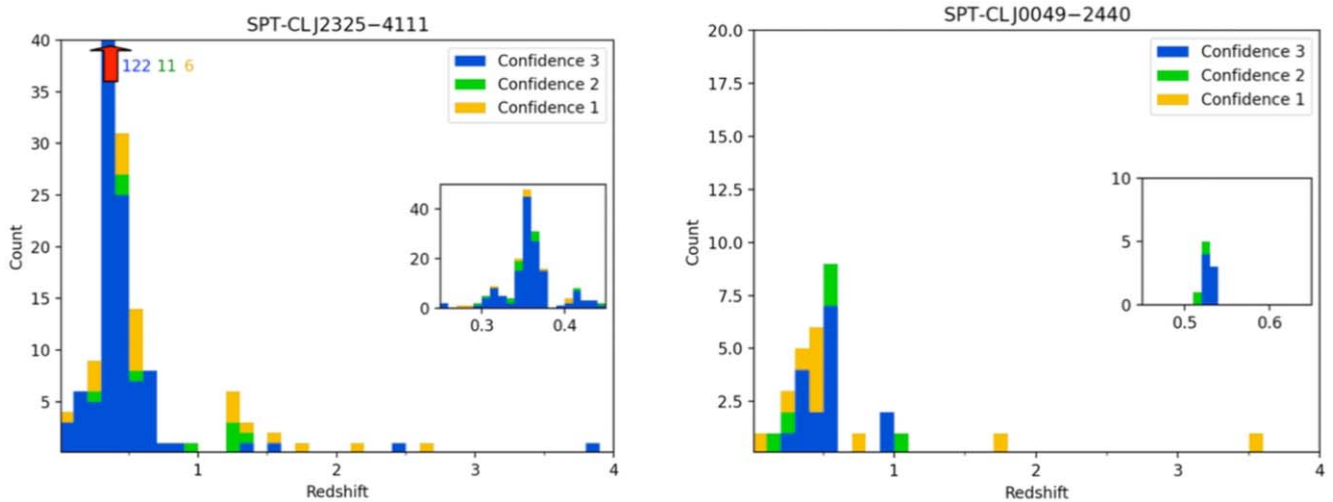


Figure 3. Redshift histogram of all the objects with spectroscopic redshift measurements in the field of view of SPT-CL J2325–4111 (left) and SPT-CL J0049–2440 (right). The redshifts are tabulated in Tables 3 and 4, respectively. The insets show a zoom-in around each cluster redshift, to illustrate the velocity structure in a narrower redshift range. The redshift bin size is $\Delta_z = 0.1$ in the main figure and $\Delta_z = 0.01$ in the insets. The different colors represent the spec- z confidence level as described in Section 2.4. For better display the left histogram is cut at 40 counts and the red arrow indicates the number of galaxies in the unique redshift bin going beyond 40.

$z = 1.318$. The lensing analysis strongly favored the $z = 1.318$ solution, resulting in a $5 \times$ lower χ^2 and a factor of 10 reduction in source plane rms. We therefore adopt this solution as the redshift of this source.

No emission lines were identified in the spectra of arcs 7.1, 8.1, and c1 at the depth of our data.

In the field of SPT-CL J0049–2440, we targeted arcs 1.2, 2.1/2.2, 4.1, and 5.1/5.2, on the first night and arcs 1.2, 1.3, 3.1, and 6.1/6.2 on the second night. We secured a spectroscopic redshift of source 1 at $z = 3.022$ from O III. In arcs 6.1/6.2, we observed a faint line at 16869 \AA , which could be either O III 5008 at $z = 2.368$ or $H\alpha$ at $z = 1.570$. We produced lens models for both solutions, and found that the lens model that used the lower redshift as constraint failed to produce the observed radial arc at the observed position, and generated predicted counter-images for this arc that are not observed in the data. We therefore proceed with a redshift of $z = 2.368$ for this arc.

Spectra of the other targeted arcs in SPT-CL J0049–2440 did not yield emission lines. Since the spectrum of arc 1.3 did not confirm it as a counter-image of arc 1.2, we did not use it as constraint in the lens model.

2.4. Spectroscopic Redshift Measurements and Redshift Catalogs

We extracted redshifts from the observed LDSS3, IMACS, and FIRE spectra as follows. We convolved the reduced 2D spectra with a 1D Gaussian profile along the wavelength axis. The Gaussian parameters were fit to a stack of spectra of a manually selected clean part of the slit, to increase the signal-to-noise ratio (S/N) and derive robust values. The spectra are not strictly perpendicular to the slit; ignoring any higher-order distortion, we extracted the 1D spectra along a manually adjusted linear trace on the wavelength axis. The redshift assessment was performed by matching spectral features to the most common emission and absorption lines.

We assigned a confidence level to each spec- z based on the number and strength of spectral features according to the following rules:

1. Confidence 3: secure redshift, with several strong spectral features.
2. Confidence 2: probable redshift, relying on one emission line or several faint absorption features.
3. Confidence 1: tentative redshift, relying on one spectral feature with low S/N.

We complemented our final catalog with the reported GMOS spectroscopy measurements for SPT-CL J2325–4111 from M. B. Bayliss et al. (2016). For sources that were measured by multiple instruments, we report the highest confidence measurement, where GMOS has the highest confidence, followed by FIRE, LDSS3, and IMACS. Our final catalog for SPT-CL J2325–4111 contains 230 galaxies, of which 224 are not multiple images of lensed sources, and for SPT-CL J0049–2440 we have spectroscopic redshifts for 29 galaxies in the field, and redshifts of two additional lensed sources. The non-arcs catalogs are presented in Tables 3 and 4, and redshifts of strongly lensed galaxies with multiple images are listed in Table 1. The redshift histograms for both cluster fields are presented in Figure 3.

3. Strong-lensing Analysis

3.1. Lens Modeling

The strong-lens models were constructed using the public lens modeling software *Lenstool* (E. Jullo et al. 2007). The algorithm uses Markov Chain Monte Carlo (MCMC) sampling to determine the best-fit model, and explores the parameter space to facilitate a statistical assessment of the uncertainties in model parameters and measurements derived from the lens model. The best solution is determined by minimizing the scatter between observed and model-predicted image-plane positions of the lensing constraints, i.e., images of lensed background galaxies.

As with many other parametric algorithms, *Lenstool* assumes that the mass distribution of the lens can be fairly described by a linear combination of halos described by a parameterized mass distribution. Several mass density profiles are implemented, e.g., isothermal, or the Navarro–Frenk–White

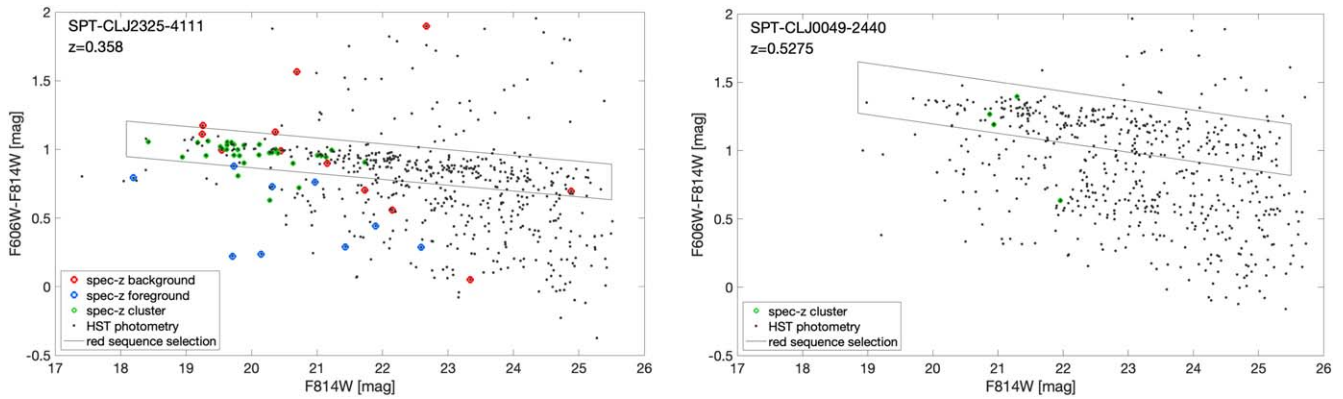


Figure 4. Color–magnitude diagrams of SPT-CL J2325–4111 (left) and SPT-CL J0049–2440 (right). HST/ACS F606W – F814W color vs. F814W magnitude is plotted in black for galaxies within the ACS field of view. Spectroscopically confirmed galaxies are color-coded by their redshift with respect to the cluster (background, foreground, or at the cluster redshift, see legend). The red-sequence selection is marked with black lines. See Section 3.2.1 for more details.

(J. F. Navarro et al. 1996) profile. In this work, we use the pseudo-isothermal ellipsoidal mass distribution (dPIE; Á. Eliasdóttir et al 2007, also referred to in the literature as PIEMD), which has an elliptical geometry, a flattened core, and a truncated isothermal slope of $\rho \propto r^{-2}$. The halo is described by seven parameters: α , δ centroid, ellipticity e , position angle θ , core radius r_{core} , truncation radius r_{cut} , and normalization σ_0 . Note that σ_0 represents a fiducial central velocity dispersion as defined in the dPIE parameterization, and is not equal to the observed velocity dispersion (for the parameterization of dPIE, and the relationship between an observed velocity dispersion and σ_0 , we refer the reader to Á. Eliasdóttir et al 2007). The mass of galaxy clusters is dominated by dark matter and may best be described by more than one dominant cluster-scale halo. Cluster-member galaxies contain a small fraction of the total cluster mass but make an important contribution to the complexity of the lensing potential. We model cluster-member galaxies as dPIE halos as well, but link their parameters more strongly to their observed stellar mass. In particular, their positional parameters (α , δ , e , θ) remain fixed to the properties of their light distribution as measured with Source Extractor (E. Bertin & S. Arnouts 1996). The slope parameters are linked to the luminosity through scaling relations (E. Jullo et al. 2007) that are optimized in the modeling process for the entire galaxy catalog as a whole. Some galaxies were optimized separately from the scaling relations, including the brightest cluster galaxies (BCGs) and other galaxies in close proximity to multiple images.

The modeling process is done iteratively, starting from the most obvious and secure lensing constraints (multiple images and arcs) to inform a preliminary lens model. The model is then used to assist in identifying more images of lensed galaxies that can be used as constraints. When each new set of constraints is added to the analysis, the modeling process is re-initiated in order to not bias the model to fixate on an early solution. Table 2 lists the optimized and fixed model parameters for each cluster, with their best-fit solutions and uncertainties as determined from the MCMC analysis.

3.2. Identification of Lensing Constraints

We used the locations of multiply imaged systems as constraints to our modeling. We identified multiple image “families” based on the morphology, color, and spectroscopic redshift. When spectroscopic redshift was not available we associated the images of the family based on color and morphology only. If the spectroscopic redshift was only

measured in a subset of the family we associated the same redshift to all images of the family. Table 1 lists all the identified lensed constraints; Figures 1 and 2 label the multiple images of each source. The coordinates of clumps within images that were used as further constraints are only listed in the table, to avoid overcluttering the figures. We used as constraints in our models only multiple images that were considered as secure. We consider a candidate to be secured when morphology, color, and lensing configurations through the iterative process converged toward being images of the same source. Candidate lensed systems are suggestive of a multiply imaged system or images within a secure system that are often too faint, or contaminated by light from a nearby galaxy, to be securely associated with lensing constraints. Although they can often be geometrically confirmed by the lens model, we exclude them from the list of constraints in order to avoid confirmation bias (see Table 1 for systems marked with a “c” and considered only as candidates).

In SPT-CL J2325–4111 we identified nine multiply imaged systems; one (system 7) is labeled as candidate and eight are considered secure. Image 6.2 is considered a candidate due to contamination from arc 1.

In SPT-CL J0049–2440 we identified nine multiply imaged systems, all of which are secure. A candidate is identified as image 3 of source 1. This system is further discussed in Section 4.3, and the attempt to spectroscopically confirm the candidate image is discussed in Section 2.3. Image 4.2 is an extended faint arc, likely affected by foreground galaxies. We consider it as a candidate as well.

3.2.1. Identification of Cluster-member Galaxies

Cluster-member galaxies were identified based on their color with respect to the cluster red sequence (M. D. Gladders & H. K. C. Yee 2000) in a color–magnitude diagram, using spectroscopic redshift information where available. The catalogs were constructed as follows. We started by running Source Extractor (E. Bertin & S. Arnouts 1996) in dual image mode, using the F814W image for identification and measuring the F814W MAG_AUTO and F606W – F814W color within the same detection apertures. We flagged and removed stars and artifacts based on their location in a MU_MAX versus MAG_AUTO space. We then matched the coordinates of the photometric and spectroscopic catalogs. For SPT-CL J2325–4111, where numerous objects with spectroscopic redshifts are within the HST field of view, we fit a line to the F606W – F814W color versus

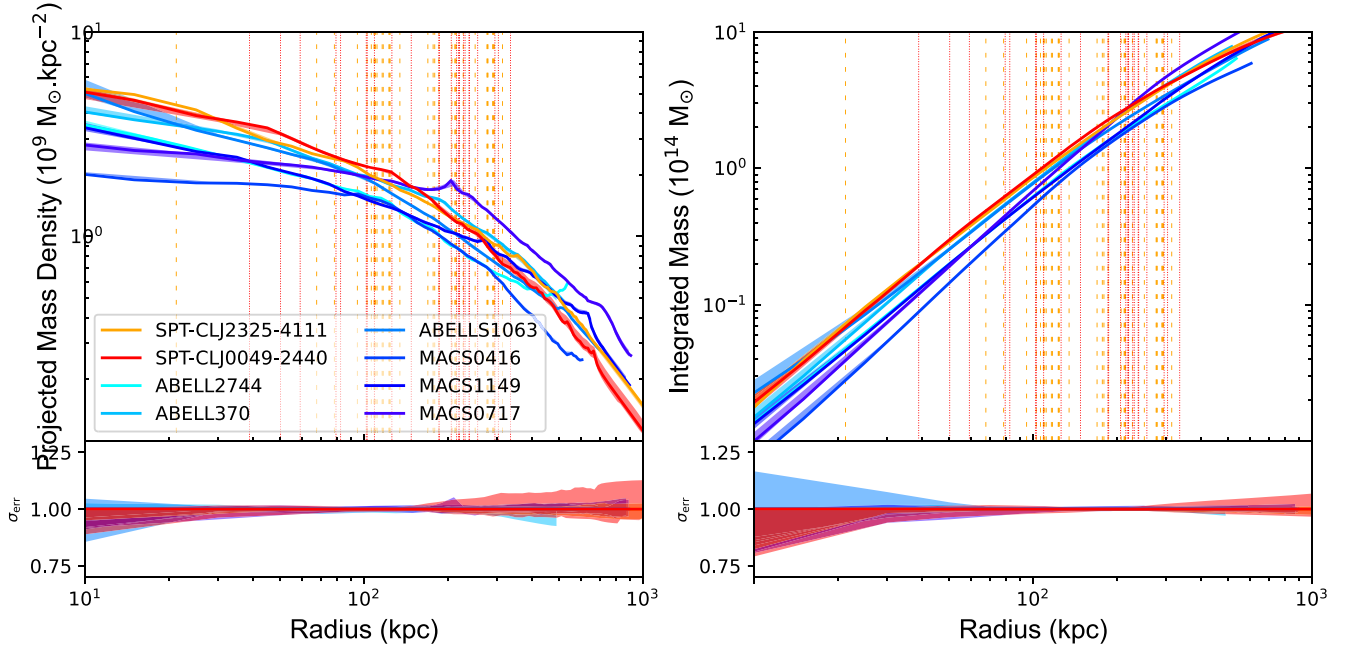


Figure 5. Projected mass density profiles (left) and cumulative projected mass profiles (right) of SPT-CL J2325–4111 (orange) and SPT-CL J0049–2440 (red) plotted against distance from the BCG. Vertical dashed orange and dotted red lines mark the position of multiple images for SPT-CL J2325–4111 and SPT-CL J0049–2440, respectively. The six Frontier Fields clusters are plotted for comparison. The mass profiles of the two clusters studied in this work have higher density than the Frontier Fields in the innermost ~ 200 kpc, and comparable density and large-scale mass at larger radii.

F814W magnitude of cluster members (those within $\Delta z = 0.03$ of the cluster redshift) using iterative 3σ clipping, which successfully removes blue cluster-member galaxies from the fit. We set the red-sequence selection as 5σ above and below the fit, with a faint-end limit of 25.5 mag and a bright-end limit set by the magnitude of the BCG, to account for intrinsic scatter in the red sequence and reduce contamination from faint field galaxies. The model of SPT-CL J2325–4111 includes 277 cluster-member galaxies, of which six were optimized separately from the scaling relations; the model of SPT-CL J0049–2440 includes 224 cluster members, two of which were optimized separately, as listed in Table 2. The color–magnitude diagrams are shown in Figure 4. Spectroscopically confirmed cluster members, and foreground and background galaxies within the ACS field of view, are marked in color.

3.2.2. Lens Modeling Results

The lensing analysis of these lines of sight resulted in two well-calibrated “cosmic telescopes,” as indicated by the low image-plane scatter between observed and predicted images of lensed sources: $\text{rms} = 0.''63$ for SPT-CL J2325–4111 and $\text{rms} = 0.''73$ for SPT-CL J0049–2440.

The image-plane rms reflects the ability of the best-fit lens models to describe the lensing potential and reproduce the lensing evidence. A high rms could imply that the underlying mass distribution is more complex than what is permitted by the flexibility of the parameterized modeling. On the other hand, a very low rms could point to overfitting. Our results are in the same range as those for other clusters with similar richness of lensing evidence in the literature (e.g., J. Richard et al. 2011; A. Zitrin et al. 2017; C. Cerny et al. 2018). In addition to the overall rms, we report in Table 1 an indicator of goodness of fit for each image, in the form of the distance between its observed and predicted positions. These values

highlight which systems and images perform better and help assess the fidelity of the model.

Figures 1 and 2 show the critical curves for a source at $z = 2$ for the best-fit model of each cluster. We confirm the initial assessment that both of these clusters have a massive core, as indicated by the large separation between the giant arcs and the BCG. We measured the effective Einstein radius of each cluster, defined as $\theta_E = \sqrt{A/\pi}$, where A is the area of an ellipse fit to the tangential critical curve. For a source at the redshift of the most prominent giant arc in SPT-CL J2325–4111, we measured $\theta_E(z = 1.579) = 32''$, whereas for a generic $z = 9$ source plane we measured $\theta_E(z = 9) = 42''$. Similarly, for SPT-CL J0049–2440 the effective Einstein radii are $\theta_E(z = 3.022) = 36''$ and $\theta_E(z = 9) = 43''$.

The clusters are generally well-represented by one cluster-scale halo ($\sigma_0 > 1000 \text{ km s}^{-1}$), with contribution from a high-mass galaxy-scale halo ($\sigma_0 \gtrsim 500 \text{ km s}^{-1}$) near the cluster core, and the rest are more typical cluster-member galaxies. The best-fit parameters of the lens models and their 68%-ile upper and lower limits are tabulated in Table 2. As part of the lensing analysis, the minimization process also solves for the unknown redshifts of multiply imaged lensed sources that were used as constraints. These are reported in Table 1 as median \pm 68%-ile, determined directly from the MCMC sampling of the parameter space.

We also calculated the lensing magnification and the projected mass density map of each cluster. Uncertainties of these lensing outputs were derived from the MCMC sampling of the parameter space, by selecting 100 steps from the chain at random, and producing the relevant mass and magnification outputs for each of these realizations of the model. We note that the statistical uncertainties underestimate the true uncertainty and do not take into account systematic errors (see M. Meneghetti et al. 2017 for a detailed discussion, and T. L. Johnson & K. Sharon 2016 for a quantitative assessment of systematic uncertainties as related to the number of arcs and spectroscopic redshifts).

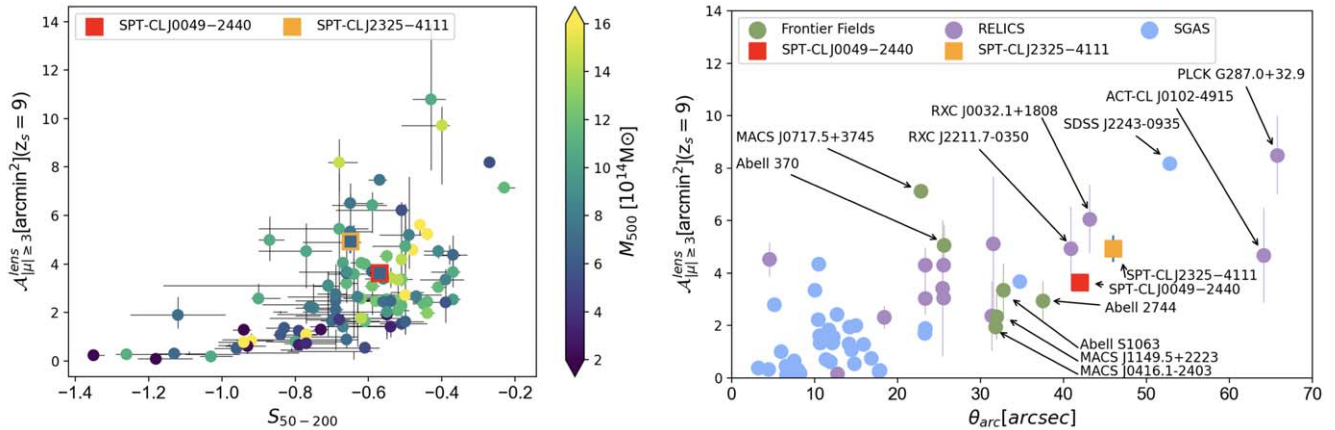


Figure 6. Left: lensing strength $A_{|\mu| \geq 3}^{\text{lens}}$ plotted against the central slope of the projected mass density profile (S_{50-200}). The data points are color-coded by their M_{500} mass. The comparison sample is from C. Fox et al. (2022) and references therein. The SPT-CL J2325–4111 and SPT-CL J0049–2440 data points are highlighted with orange and red edges, respectively, with their M_{500} adopted from S. Bocquet et al. (2019) and L. E. Bleem et al. (2020). These two clusters have relatively high lensing strength compared to other clusters with similar properties. Right: lensing strength plotted against the projected separation between the farthest bright arc and the BCG, compared to strong-lensing cluster samples. The error bars reflect the systematic uncertainties, determined from the range of measurements obtained by different lens modeling algorithms, where available. Notably, SPT-CL J2325–4111 and SPT-CL J0049–2440 have similar lensing strengths to the Frontier Fields. Figures adapted from C. Fox et al. (2022).

Table 1 lists the model-predicted magnification at the observed location of each arc. For arcs without a spectroscopic redshift, the predicted magnification of each realization was calculated for the redshift parameter associated with the same step in the MCMC chain. We discuss the results in the following sections.

4. Discussion

4.1. Mass Profiles and Substructures

Given the large radial extent of the lensing constraints in these lines of sight, we can accurately measure the total enclosed projected mass density out to relatively large radii. The core mass of SPT-CL J2325–4111, measured within 500 kpc, is $M(<500 \text{ kpc}) = (7.30 \pm 0.07) \times 10^{14} M_{\odot}$, and the core mass of SPT-CL J0049–2440 is $M(<500 \text{ kpc}) = 7.12_{-0.19}^{+0.16} \times 10^{14} M_{\odot}$.

Figure 5 shows the projected mass density profiles of SPT-CL J2325–4111 and SPT-CL J0049–2440 in the left panel, and the cumulative enclosed mass as a function of clustercentric radius in the right panel. In both plots, the distances are measured from the BCG of each cluster. For comparison, we plot on the same figures the density profiles and cumulative mass profiles of the six Frontier Fields clusters (J. M. Lotz et al. 2017), which we derived from the public `Lenstool` models of these clusters (Sharon V4¹⁵). We find that at projected radii beyond ~ 200 kpc, the density profiles and cumulative enclosed mass of both clusters are comparable to those of the average Frontier Fields cluster. However, closer to the cluster cores ($R < 200$ kpc), both clusters have higher mass density profiles than the Frontier Fields clusters (left panel of Figure 5). This mass distribution may provide an explanation for the high lensing efficiency of SPT-CL J2325–4111 and SPT-CL J0049–2440, consistent with the association of clusters with higher concentration with higher lensing efficiency (C. Giocoli et al. 2012).

Parametric lens modeling algorithms such as `Lenstool` can separate the contributions to the lensing potential from the different mass components, to calculate the fraction of mass contained in substructures and galaxy-scale halos. We estimate

the substructure mass by removing Halo 1, which represents the cluster-scale dark matter halo (see Table 2), and measure the total projected mass density within 500 kpc associated with the remaining halos. We find that the substructure mass of SPT-CL J2325–4111 amounts to a fraction of 0.12 ± 0.01 of the total mass, and in SPT-CL J0049–2440, the substructure amounts to $0.21_{-0.05}^{+0.07}$ of the total mass (median and 68% uncertainty as derived from the MCMC sampling). Previous studies reported amounts as low as 0.01 (G. Mahler et al. 2019) and as high as 0.3 (K. Sharon et al. 2020) of the total mass found in substructures. As shown by J. Richard et al. (2011), using a sample of 20 clusters, substructure mass ratios range from 0.02 to 0.78 with a median at 0.135. The strong-lensing efficiency of subhalos in the context of predictions from the cosmological model (Λ CDM) has been discussed in previous studies; see, e.g., C. Grillo et al. (2015), E. Munari et al. (2016), P. Natarajan et al. (2017), M. Meneghetti et al. (2020, 2022, 2023), Y. M. Bahé (2021), A. Robertson (2021), and Y. M. Tokayer et al. (2024) for more in-depth discussions of its impact.

4.2. Lensing Strength

C. Fox et al. (2022) studied the “lensing strength” of 74 strong-lensing clusters with public lens models and space-based imaging data available at the time. They defined the lensing strength as the total image-plane area in which a source at $z = 9$ is magnified by a factor of 3 or above. They found that the lensing strength depends somewhat on the cluster mass, and more strongly on the inner slope of the projected mass density, where a shallower inner slope can produce more powerful lenses. They also demonstrated that the Einstein radius and the projected distance between the farthest bright arc and the BCG are good predictors of lensing strength.

To contextualize the two clusters with respect to the clusters studied by C. Fox et al. (2022), we calculated the lensing strength of these clusters, finding $A_{|\mu| \geq 3}^{\text{lens}} = 4.93_{-0.04}^{+0.03} \text{ arcmin}^2$ for SPT-CL J2325–4111 (i.e., an area of $\sim 4.9 \text{ arcmin}^2$ is magnified by a factor of 3 or higher for a source at $z = 9$), and $A_{|\mu| \geq 3}^{\text{lens}} = 3.64_{-0.10}^{+0.14} \text{ arcmin}^2$ for SPT-CL J0049–2440. Following C. Fox et al. (2022), we also measured the inner slope of the mass density

¹⁵ <https://archive.stsci.edu/prepds/frontier/>

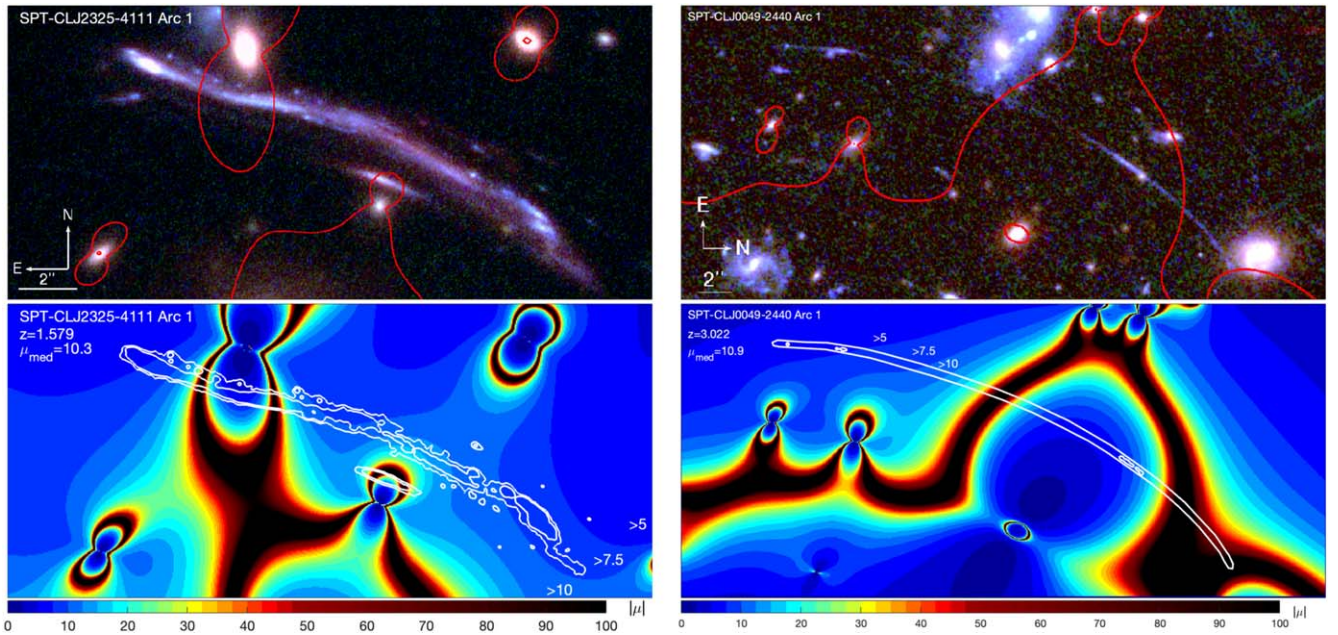


Figure 7. Zoom-in on arc 1 in SPT-CL J2325–4111 (left) and on arc 1 in SPT-CL J0049–2440 (right). Top: color composite (same data as Figures 1 and 2) showing the extent of the giant arc. Critical curves for the arc redshift are overlaid in red. Bottom: map of absolute magnification within the same field of view, computed from the best-fit lens model for the redshift of the arc. The color bar at the bottom indicates the absolute magnification values. The white contours indicate the location of the giant arcs, which span a wide range of magnifications. The median magnification within the contour is 10.3 and 10.9 for SPT-CL J2325–4111 and SPT-CL J0049–2440, respectively. Note that the field of SPT-CL J0049–2440 is rotated by 90° and less zoomed-in; see compass and scale bar at the bottom left of each imaging panel for reference. Because the arc in this field is faint, the color composite was smoothed with a 3 pixel Gaussian kernel, and the external contours were placed manually to guide the eye.

profile derived from the lens models, S_{50-200} , which is defined as the log of the slope of density profile measured between 50 and 200 kpc from the BCG, finding $S_{50-200} = -0.59_{-0.56}^{-0.62}$ for SPT-CL J0049–2440 and $S_{50-200} = -0.67_{-0.66}^{-0.69}$ for SPT-CL J2325–4111. In Figure 6 we compare the two clusters to a large sample of strong-lensing clusters from C. Fox et al. (2022) that span a wide range of cluster properties, including clusters from SGAS (K. Sharon et al. 2020), RELICS (D. Coe et al. 2019), and Frontier Fields (J. M. Lotz et al. 2017). The left panel shows the $\mathcal{A}_{|\mu| \geq 3}^{\text{lens}} - S_{50-200}$ plane, and the right panel shows the lensing strength as a function of separation between the farthest bright arc and the BCG. We find that SPT-CL J2325–4111 and SPT-CL J0049–2440 have a higher lensing strength than most clusters with similar M_{500} or inner slope, consistent with their observed large θ_{arc} separation; they appear to have a lensing strength comparable to the Frontier Fields.

4.3. Lensed Sources of Interest

Each of the clusters studied in this work lenses numerous sources, which were used to constrain the lens model. While not the focus of this analysis, we highlight two prominent arcs observed in these fields. In SPT-CL J2325–4111, the image of Source 1, “J2325 arc 1” ($z = 1.579$), appears as a bright 18'' long giant arc north of the cluster core, with observed magnitude of $m_{\text{AB}} = 19.2$ (19.1) in the F606W (F814W) band. The multiplicity of the arc was not immediately obvious: it appears that most of the arc is singly imaged into a high-distortion arc, where only regions next to the nearby cluster-member galaxy are multiple images of a small region of the source galaxy. A set of star-forming clumps can be mapped with mirror symmetry about the critical curve (Figure 7). The bright core of the galaxy in the east end of the arc and the long red tail to the west are singly imaged. The bottom panel of

Figure 7 shows the magnification map from the best-fit lens model. We estimate a median magnification along the arc of $\mu_{\text{med}} = 10.3$; in most regions the arc is magnified by at least a factor of 8, with areas very close to the critical curve being magnified by more than 50. The brightness, prominent clumps, and indication of more details in the infrared make this arc a promising target for study by JWST.

The highly extended arc in SPT-CL J0049–2440, “J0049 arc 1” ($z = 3.022$), spans 31'' in the image plane. It is much fainter, and most likely composed of two or three images along the arc. The most likely counter-images (labeled 1.3 and 1.4 in Figure 2) have comparable local magnification but do not suffer from the high distortion of the giant arc. The morphology and image-plane size of the counter-images indicate that the source galaxy is quite compact; we measure an FWHM of $0''.19$ for image 1.3 using IRAF, which translates to $0.49_{-0.02}^{+0.04}$ kpc in the source plane after dividing by the square root of the lensing magnification. A separate clump, or companion galaxy, is observed nearby ($< 0''.5$ in the image plane), labeled as source 1.x.2 in Table 1. Figure 7 shows a zoom-in on the faint giant arc and the lensing magnification. We estimate a median magnification of $\mu_{\text{med}} = 10.9$ along the arc. Table 1 lists the measured magnifications and their uncertainties at the positions along the arc and counter-images that were used as lensing constraints. Deep, high-resolution imaging with JWST could reveal substructures within this galaxy on a subkiloparsec scale, given its extreme tangential distortion and its large extent in the image plane.

5. Summary

We present strong-lensing models of two clusters, SPT-CL J2325–4111 and SPT-CL J0049–2440, based on multi-band HST imaging and spectroscopic redshifts from Magellan/

LDSS3, Magellan/FIRE, and Gemini/GMOS. We report the following.

1. The projected mass of SPT-CL J2325–4111 within 500 kpc from the BCG is $M(< 500 \text{ kpc}) = (7.30 \pm 0.07) \times 10^{14} M_{\odot}$ (cylindrical mass), with a subhalo mass ratio of 0.12 ± 0.01 . The projected mass of SPT-CL J0049–2440 is $M(< 500 \text{ kpc}) = 7.12^{+0.16}_{-0.19} \times 10^{14} M_{\odot}$ (cylindrical mass), with a subhalo mass ratio of $0.21^{+0.07}_{-0.05}$. A comparison of the projected mass density profiles of these clusters to those of other strong lenses indicates a higher density within the innermost few hundred kiloparsecs than that of the Frontier Fields clusters.
2. The Einstein radii for a source at $z = 9$ as measured from the lens models are $42''$ and $43''$ for SPT-CL J2325–4111 and SPT-CL J0049–2440, respectively.
3. Following C. Fox et al. (2022), we measured the area magnified by a factor of $\mu \geq 3$ for a source at $z = 9$ (i.e., lensing strength) as $\mathcal{A}_{|\mu| \geq 3}^{\text{lens}} = 4.93^{+0.03}_{-0.04} \text{ arcmin}^2$ and $\mathcal{A}_{|\mu| \geq 3}^{\text{lens}} = 3.64^{+0.14}_{-0.10} \text{ arcmin}^2$ for SPT-CL J2325–4111 and SPT-CL J0049–2440, respectively.
4. We report on two giant arcs of highly magnified sources in these fields. “J2325 arc 1” ($z = 1.5790$) is projected $\theta_{\text{arc}} = 46''$ north of the BCG of SPT-CL J2325–4111, spanning $18''$ in the image plane, with a median magnification of $\mu_{\text{med}} = 10.3$. “J0049 arc 1” ($z = 3.0220$) is projected $\theta_{\text{arc}} = 42''$ northeast of the BCG of SPT-CL J0049–2440, spanning $31''$ in the image plane, with a median magnification of $\mu_{\text{med}} = 10.9$. Their high distortions indicate promising resolving capabilities for detailed morphological analysis of galaxies at cosmic noon.

We conclude that the lensing power measured at these strong-lensing sightlines promotes SPT-CL J2325–4111 and SPT-CL J0049–2440 to the top tier of strong-lensing clusters known today, on par with well-studied clusters such as the Frontier Fields; these clusters have yet untapped potential for follow-up studies of the high-redshift Universe they magnify.

Acknowledgments

This research is based on observations made with the NASA/ESA Hubble Space Telescope obtained from the Space Telescope Science Institute, which is operated by the Association of Universities for Research in Astronomy, Inc., under NASA contract NAS 5-26555. These observations are associated with program(s) HST-GO-15937. Support for HST program #15937 was provided by NASA through a grant from the Space Telescope Science Institute, which is operated by the Association of Universities for Research in Astronomy, Inc., under NASA contract NAS 5-03127. The HST data presented in this article were obtained from the Mikulski Archive for Space Telescopes (MAST) at the Space Telescope Science Institute. The specific observations analyzed can be accessed

via DOI:[10.17909/5gpg-5575](https://doi.org/10.17909/5gpg-5575). This paper includes data gathered with the 6.5 m Magellan Telescopes located at Las Campanas Observatory, Chile. NOIRLab IRAF is distributed by the Community Science and Data Center at NSF NOIRLab, which is managed by the Association of Universities for Research in Astronomy (AURA) under a cooperative agreement with the U.S. National Science Foundation. The South Pole Telescope program is supported by the National Science Foundation (NSF) through award OPP-1852617. Partial support is also provided by the Kavli Institute of Cosmological Physics at the University of Chicago. Work at Argonne National Lab is supported by UChicago Argonne LLC, Operator of Argonne National Laboratory (Argonne). Argonne, a U.S. Department of Energy Office of Science Laboratory, is operated under contract no. DE-AC02-06CH11357.

Facilities: HST (ACS, WFC3), Magellan:Clay, Magellan:Baade.

Software: Source Extractor (E. Bertin & S. Arnouts 1996); Lenstool (E. Jullo et al. 2007); NOIRLab IRAF v2.18 (M. Fitzpatrick et al. 2024); AstroDrizzle (A. S. Fruchter et al. 2010); Matlab (Mathworks Inc. 2022); Astropy (Astropy Collaboration et al. 2013, 2018, 2022); MATLAB Astronomy and Astrophysics Toolbox (MAAT; E. O. Ofek 2014).

Appendix A Spectroscopic Catalogs

We provide in this appendix spectroscopic catalogs of all the objects in SPT-CL J2325–4111 and SPT-CL J0049–2440 for which spectroscopic redshifts were measured, as described in Section 2.3. We report them in Tables 3 and 4. For strongly lensed galaxies, see Table 1.

Table 3
List of the 224 Spectroscopically Identified Objects in the Field of View of SPT-CL J2325–4111

ID	R.A. J2000	Decl. J2000	z_{spec}	Conf.	Instruments
01401	351.3441640	−41.2209030	0.348900	3	GMOS
01413	351.3497470	−41.1972200	0.160000	3	GMOS
01390	351.3407030	−41.1987940	0.361300	3	GMOS
01368	351.3332750	−41.1982170	0.363900	3	GMOS
01265	351.3085740	−41.2348110	0.363800	3	GMOS
01336	351.3243450	−41.2229620	0.352100	3	GMOS
01218	351.2987820	−41.2038280	0.362400	3	GMOS
01201	351.2953760	−41.1707570	0.192000	3	GMOS
01318	351.3188660	−41.1687860	0.357900	3	GMOS
01241	351.3030290	−41.1961540	0.356700	3	GMOS

Note. Spectroscopic redshifts measured in SPT-CL J2325–4111 are from Gemini, Magellan/LDSS3, and Magellan/IMACS. See Section 2.3 for details of the spectroscopic analysis. Strongly lensed galaxies are tabulated in Table 1. (This table is available in its entirety in machine-readable form in the [online article](#).)

Table 4

List of Spectroscopically Identified Objects in the Field of View of SPT-CL J0049–2440

ID	R.A. J2000	Decl. J2000	z_{spec}	Conf.	Instruments
030	12.2958676	−24.6396331	0.3445	1	LDSS3
025	12.2976676	−24.6445438	0.2752	2	LDSS3
024	12.2947339	−24.6482300	0.5279	3	LDSS3
027	12.3155564	−24.6437909	0.5318	3	LDSS3
023	12.2940359	−24.6542052	0.2492	3	LDSS3
026	12.3073222	−24.6526637	0.3426	3	LDSS3
028	12.3072829	−24.6551361	0.3448	3	LDSS3
022	12.2909294	−24.6640596	0.4341	3	LDSS3
006	12.2876854	−24.6674970	0.4440	1	LDSS3
010	12.2893727	−24.6700378	0.0	1	LDSS3
011	12.2751750	−24.6766800	0.9398	3	LDSS3
004	12.3026499	−24.6699485	0.746	1	LDSS3
002	12.2849216	−24.6888735	1.0302	2	LDSS3
001	12.2888840	−24.6913042	0.4299	1	LDSS3
009	12.2985897	−24.6906095	0.5355	3	LDSS3
005	12.3041248	−24.6907131	1.72	1	LDSS3
012	12.3042900	−24.6931631	0.5293	3	LDSS3
013	12.2957763	−24.6986553	0.5321	3	LDSS3
014	12.2821687	−24.7062031	0.5265	3	LDSS3
015	12.2867523	−24.7068513	0.5185	2	LDSS3
034	12.2776163	−24.7128064	0.3572	3	LDSS3
017-A	12.3229906	−24.7002583	0.3141	3	LDSS3
017-B	12.3227230	−24.6997445	0.2482	1	LDSS3
016	12.3205370	−24.7033231	0.4047	3	LDSS3
018	12.2758188	−24.7225908	0.1910	2	LDSS3
020	12.3018904	−24.7172519	0.9065	3	LDSS3
019	12.2965644	−24.7212467	0.437	1	LDSS3
021	12.3004454	−24.7249998	0.5247	3	LDSS3
033	12.3159975	−24.7222300	0.5234	2	LDSS3
032	12.3054420	−24.7283286	0.4038	1	LDSS3

Note. Spectroscopic redshifts measured in SPT-CL J0049–2440 are from Magellan/LDSS3. See Section 2.3 for details of the spectroscopic analysis. Strongly lensed galaxies are tabulated in Table 1. 017-A and 017-B are two different galaxy detections from the same slit, ID017.

Appendix B

SPT-CL J0512–3848

A third cluster, SPT-CL J0512–3848, was flagged as a promising strong-lens candidate as part of our HST program to identify the next generation of extraordinary cluster lenses (GO-15937; PI: G. Mahler). The cluster was cataloged by L. E. Bleem et al. (2020) with significance $\xi = 7.54$, $z = 0.326$, and $M_{500c} = 6.07^{+0.87}_{-0.88} \times 10^{14} h_{70}^{-1} M_{\odot}$. Ground-based optical imaging with Magellan/PISCO revealed promising arclike features (see Figure 8 of L. E. Bleem et al. 2020). Despite the preliminary evidence, the combined analysis of HST morphology and extensive LDSS3 spectroscopy indicated that most of the arclike features are high-flexure singly imaged lensed

Table 5

List of Spectroscopically Identified Objects in the Field of View of SPT-CL J0512–3848

ID	R.A. J2000	Decl. J2000	z_{spec}	Conf.	Instruments
1	78.2523417	−38.7977722	1.420	3	LDSS3
2	78.2634083	−38.7980306	1.200	2	LDSS3
3	78.2550625	−38.7866944	0.9187	3	LDSS3
4	78.2330458	−38.7893667	1.337	3	LDSS3
5	78.2295042	−38.7903139	1.329	3	LDSS3
6	78.2595542	−38.7952194	0.334	3	LDSS3
7	78.2625458	−38.7988722	1.046	3	LDSS3
8	78.2646458	−38.7992667	0.32	2	LDSS3
9	78.2530417	−38.7862778	1.186	3	LDSS3
10	78.2343458	−38.7863167	1.146	3	LDSS3
11	78.2421125	−38.7858972	1.059	2	LDSS3
12	78.2355625	−38.7840167	0.471	2	LDSS3
13	78.2381708	−38.7813083	1.049	3	LDSS3
14	78.2490208	−38.7816333	1.036	3	LDSS3
15	78.2522458	−38.7811111	0.516	3	LDSS3
16	78.2466083	−38.7804389	1.490	3	LDSS3
17	78.2636375	−38.7742222	0.872	3	LDSS3
18	78.2345424	−38.7913338	0.679	3	LDSS3
19	78.2309167	−38.7915861	1.334	3	LDSS3
20	78.2320000	−38.7961528	1.333	3	LDSS3
21	78.2424292	−38.7990694	0.322	3	LDSS3
22	78.2190708	−38.7897111	0.513	3	LDSS3
23	78.2145583	−38.7762639	0.324	3	LDSS3
24	78.2255500	−38.8050750	0.895	3	LDSS3
25	78.2218708	−38.8072361	0.444	3	LDSS3
26	78.2558125	−38.8102667	1.607	2	LDSS3
27	78.2717333	−38.7909111	0.322	3	LDSS3
28	78.2491579	−38.7886275	0.928	3	LDSS3
29	78.2401483	−38.7857283	1.0604	3	LDSS3
30	78.2311376	−38.7942000	0.936	3	LDSS3
31	78.2314275	−38.7897544	0.84	3	LDSS3

Note. Spectroscopic redshifts measured in SPT-CL J0512–3848 are from Magellan/LDSS3. See Section 2.3 for details of the spectroscopic analysis.

galaxies at $z < 2$. While the cluster is likely a strong lens, there is not sufficient evidence for a robust lens model. In particular, we do not identify secure cluster-wide multiply imaged systems. The field was observed with MOS masks on 2017 January 1, 2017 January 30, 2017 September 2, 2018 January 9–10, and 2020 January 23 (J. D. Remolina González 2021, Table D.1). Data reduction and spectroscopic analysis were as described in Section 2.3. In this appendix, we provide the LDSS3 spectroscopic redshifts we obtained in this field, to facilitate possible future investigations of this line of sight by the community. Galaxies with spectroscopic redshifts at the core of SPT-CL J0512–3848 are labeled in Figure 8, overplotted on the HST imaging from GO-15937. Table 5 presents the spectroscopic redshifts of all the objects in the field observed using Magellan/LDSS3 instruments as part of the follow-up of SPT clusters, out to ~ 2.5 from the BCG.

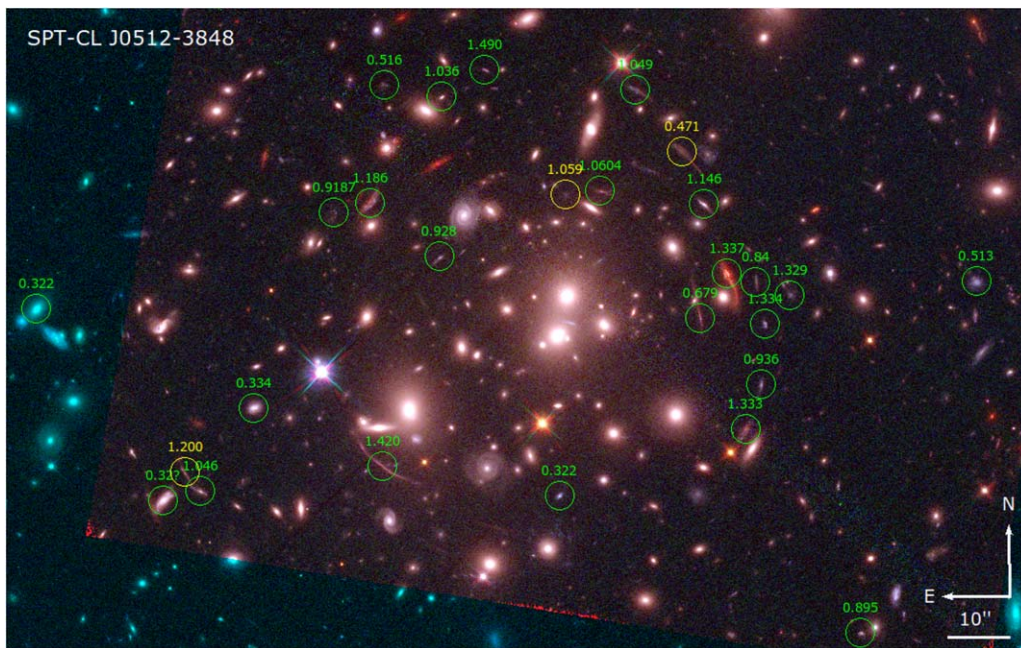
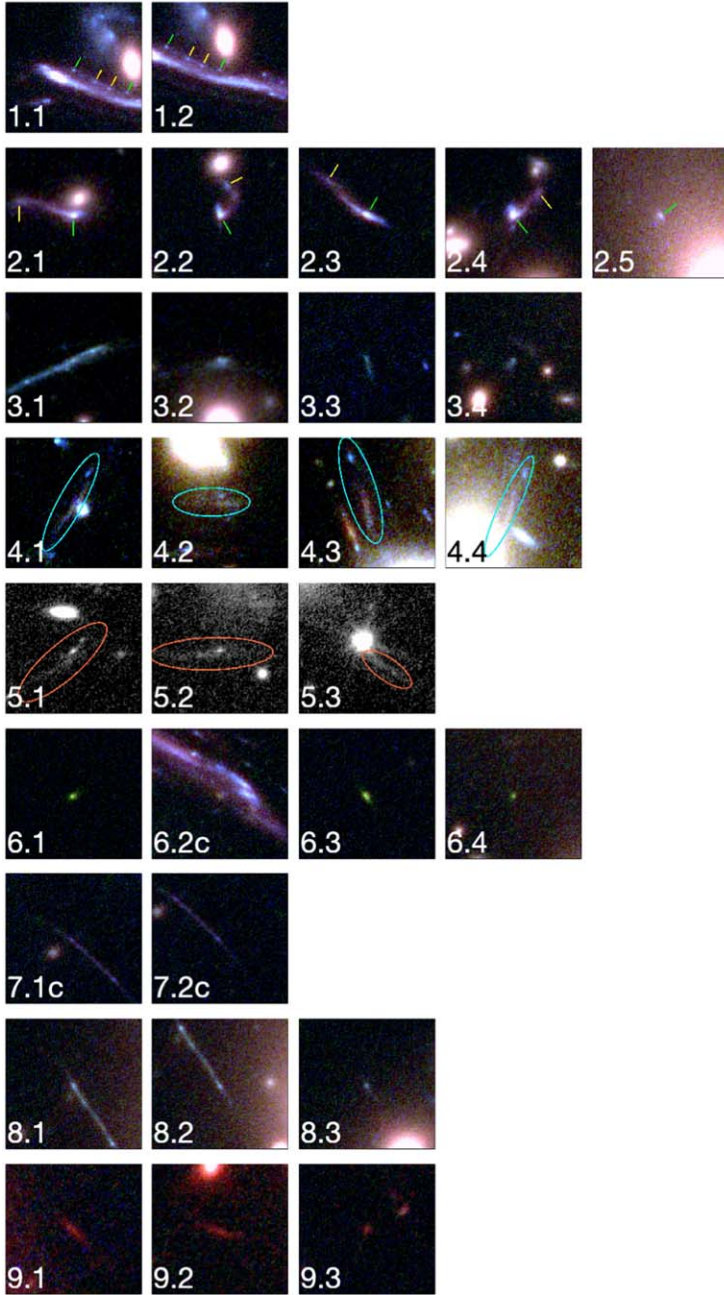


Figure 8. Composite color images of the field of SPT-CL J0512–3848, from HST imaging in WFC3-IR/F140W (red), ACS/F814W (green), and ACS/F606W (blue). Circles label the spectroscopic redshifts identified. Green circles correspond to high-confidence identification while yellow circles mark tentative redshift identification. The full list of identifications is given in Table 5.

Appendix C Lensing Candidates

In this appendix we provide a zoom-in view of the multiple images identified in this work and used as lens modeling constraints, in Figure 9. See Table 1 for coordinates, and Figures 1 and 2 for the full field of view of each cluster with arcs labeled. Section 3.2 describes the identification.

SPT-CLJ2325-4111



SPT-CLJ0049-2440

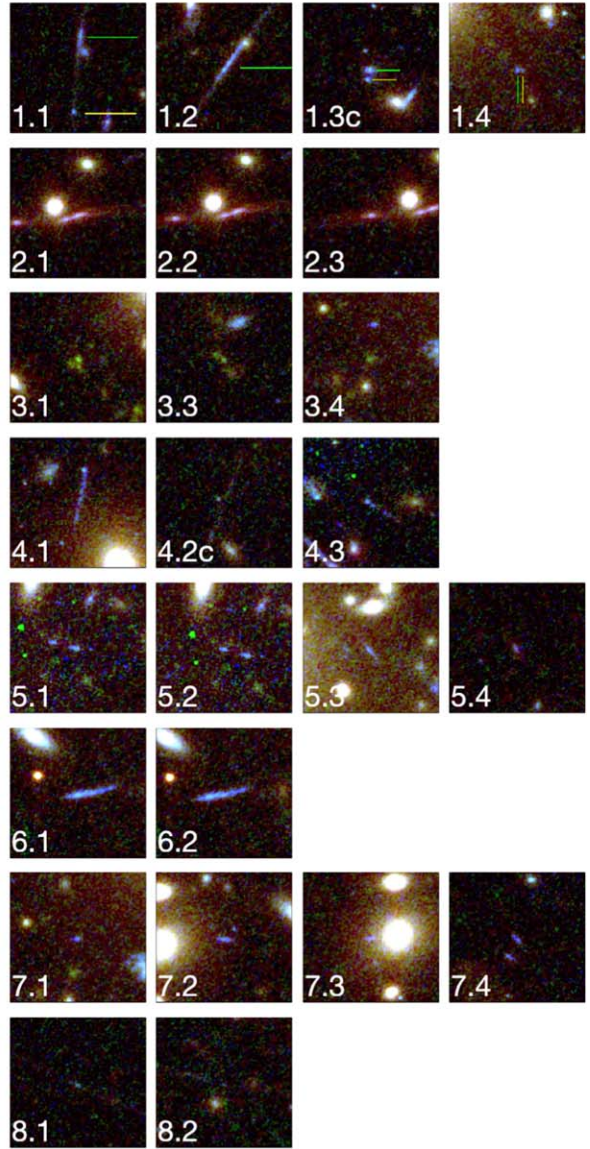


Figure 9. Zoom-in on the multiple images of lensed galaxies in SPT-CL J2325-4111 (left) and SPT-CL J0049-2440 (right). Each square has a $3'' \times 3''$ field of view, with the exception of images of sources 4 and 5 in SPT-CL J2325-4111, which are $4'' \times 4''$. Most images are centered on the clump that was identified as a constraint. In SPT-CL J2325-4111 source 4, the blue emission knot at the north of each arc was used as the constraint. The color rendition is the same as in Figures 1 and 2. For SPT-CL J2325-4111 source 5, we show only F814W in grayscale, since image 5.3 of the source is affected by diffraction spikes of a nearby star in the other bands. Green and yellow ticks mark the first and second clumps, respectively, in systems where multiple clumps were used as constraints.

ORCID iDs

Guillaume Mahler <https://orcid.org/0000-0003-3266-2001>
 Keren Sharon <https://orcid.org/0000-0002-7559-0864>
 Matthew Bayliss <https://orcid.org/0000-0003-1074-4807>
 Lindsey. E. Bleem <https://orcid.org/0000-0001-7665-5079>
 Mark Brodwin <https://orcid.org/0000-0002-4208-798X>
 Benjamin Floyd <https://orcid.org/0000-0003-4175-571X>
 Michael D. Gladders <https://orcid.org/0000-0003-1370-5010>
 Gourav Khullar <https://orcid.org/0000-0002-3475-7648>

Juan D. Remolina González <https://orcid.org/0000-0002-7868-9827>
 Arnab Sarkar <https://orcid.org/0000-0002-5222-1337>

References

Acebron, A., Jullo, E., Limousin, M., et al. 2017, *MNRAS*, 470, 1809
 Adamo, A., Bradley, L. D., Vanzella, E., et al. 2024, *Natur*, 632, 513
 Astropy Collaboration, Price-Whelan, A. M., Lim, P. L., et al. 2022, *ApJ*, 935, 167
 Astropy Collaboration, Price-Whelan, A. M., Sipőcz, B. M., et al. 2018, *AJ*, 156, 123

- Astropy Collaboration, Robitaille, T. P., Tollerud, E. J., et al. 2013, *A&A*, **558**, A33
- Atek, H., Labbé, I., Furtak, L. J., et al. 2024, *Natur*, **626**, 975
- Atek, H., Richard, J., Kneib, J.-P., et al. 2015, *ApJ*, **800**, 18
- Bahé, Y. M. 2021, *MNRAS*, **505**, 1458
- Bayliss, M. B., Gladders, M. D., Oguri, M., et al. 2011a, *ApJL*, **727**, L26
- Bayliss, M. B., Hennawi, J. F., Gladders, M. D., et al. 2011b, *ApJS*, **193**, 8
- Bayliss, M. B., Ruel, J., Stubbs, C. W., et al. 2016, *ApJS*, **227**, 3
- Bertin, E., & Arnouts, S. 1996, *A&AS*, **117**, 393
- Bezanson, R., Labbe, I., Whitaker, K. E., et al. 2024, *ApJ*, **974**, 92
- Bleem, L. E., Bocquet, S., Stalder, B., et al. 2020, *ApJS*, **247**, 25
- Bleem, L. E., Stalder, B., de Haan, T., et al. 2015, *ApJS*, **216**, 27
- Bocquet, S., Dietrich, J. P., Schrabback, T., et al. 2019, *ApJ*, **878**, 55
- Bouwens, R. J., Oesch, P. A., Illingworth, G. D., Ellis, R. S., & Stefanon, M. 2017, *ApJ*, **843**, 129
- Cañameras, R., Nesvadba, N. P. H., Guery, D., et al. 2015, *A&A*, **581**, A105
- Caminha, G. B., Suyu, S. H., Mercurio, A., et al. 2022, *A&A*, **666**, L9
- Cerny, C., Sharon, K., Andrade-Santos, F., et al. 2018, *ApJ*, **859**, 159
- Chemerynska, I., Atek, H., Furtak, L. J., et al. 2024, *MNRAS*, **531**, 2615
- Claeysens, A., Adamo, A., Richard, J., et al. 2023, *MNRAS*, **520**, 2180
- Coe, D., Salmon, B., Bradac, M., et al. 2019, *ApJ*, **884**, 85
- Dahle, H., Gladders, M. D., Sharon, K., Bayliss, M. B., & Rigby, J. R. 2015, *ApJ*, **813**, 67
- de La Vieuville, G., Bina, D., Pello, R., et al. 2019, *A&A*, **628**, A3
- de Propriis, R., Stanford, S. A., Eisenhardt, P. R., Dickinson, M., & Elston, R. 1999, *AJ*, **118**, 719
- Diego, J. M., Kaiser, N., Broadhurst, T., et al. 2018, *ApJ*, **857**, 25
- Diehl, H. T., Buckley-Geer, E. J., Lindgren, K. A., et al. 2017, *ApJS*, **232**, 15
- Dressler, A., Bigelow, B., Hare, T., et al. 2011, *PASP*, **123**, 288
- Ebeling, H., Edge, A. C., & Henry, J. P. 2001, *ApJ*, **553**, 668
- Eliasdóttir, Á., Limousin, M., Richard, J., et al. 2007, arXiv:0710.5636
- Fischer, T. C., Rigby, J. R., Mahler, G., et al. 2019, *ApJ*, **875**, 102
- Fitzpatrick, M., Placco, V., Bolton, A., et al. 2024, arXiv:2401.01982
- Fox, C., Mahler, G., Sharon, K., & Remolina González, J. D. 2022, *ApJ*, **928**, 87
- Fruchter, A. S., et al. 2010, in STScI Calibration Workshop: Hubble after SM4, Preparing JWST, ed. S. Deustua & C. Oliveira (Baltimore, MD: STScI), 382
- Furtak, L. J., Zitrin, A., Weaver, J. R., et al. 2023, *MNRAS*, **523**, 4568
- Giocoli, C., Meneghetti, M., Ettori, S., & Moscardini, L. 2012, *MNRAS*, **426**, 1558
- Gladders, M. D., Allen, S. W., Barrientos, L. F., et al. 2019, Building the SPT-HST Legacy: Imaging Massive Clusters to $z = 1.5$, HST Proposal. Cycle 26, ID. #16017
- Gladders, M. D., & Yee, H. K. C. 2000, *AJ*, **120**, 2148
- Golubchik, M., Furtak, L. J., Meena, A. K., & Zitrin, A. 2022, *ApJ*, **938**, 14
- Gonzaga, S., Hack, W., Fruchter, A., & Mack, J. 2012, The DrizzlePac Handbook, HST Data Handbook
- Grillo, C., Rosati, P., Suyu, S. H., et al. 2018, *ApJ*, **860**, 94
- Grillo, C., Suyu, S. H., Rosati, P., et al. 2015, *ApJ*, **800**, 38
- Harvey, D., Courbin, F., Kneib, J. P., & McCarthy, I. G. 2017, *MNRAS*, **472**, 1972
- Hsiao, T. Y.-Y., Coe, D., Abdurro'uf, et al. 2023, *ApJL*, **949**, L34
- Huang, X., Storfer, C., Gu, A., et al. 2021, *ApJ*, **909**, 27
- Jauzac, M., Clément, B., Limousin, M., et al. 2014, *MNRAS*, **443**, 1549
- Jauzac, M., Jullo, E., Kneib, J.-P., et al. 2012, *MNRAS*, **426**, 3369
- Johnson, T. L., Rigby, J. R., Sharon, K., et al. 2017, *ApJL*, **843**, L21
- Johnson, T. L., & Sharon, K. 2016, arXiv:1608.08713
- Jullo, E., Kneib, J.-P., Limousin, M., et al. 2007, *NJPh*, **9**, 447
- Jullo, E., Natarajan, P., Kneib, J.-P., et al. 2010, *Sci*, **329**, 924
- Kelly, P. L., Diego, J. M., Rodney, S., et al. 2018, *NatAs*, **2**, 334
- Khullar, G., Gozman, K., Lin, J. J., et al. 2021, *ApJ*, **906**, 107
- Livermore, R. C., Finkelstein, S. L., & Lotz, J. M. 2017, *ApJ*, **835**, 113
- Lotz, J. M., Koekemoer, A., Coe, D., et al. 2017, *ApJ*, **837**, 97
- Mahler, G., Jauzac, M., Richard, J., et al. 2023a, *ApJ*, **945**, 49
- Mahler, G., Natarajan, P., Jauzac, M., & Richard, J. 2023b, *MNRAS*, **518**, 54
- Mahler, G., Sharon, K., Fox, C., et al. 2019, *ApJ*, **873**, 96
- Mahler, G., Sharon, K., Gladders, M. D., et al. 2020, *ApJ*, **894**, 150
- Mathworks Inc., The 2022, MATLAB version: 9.13.0 (R2022b), (Natick, MA: The MathWorks Inc)
- McDonald, M., Allen, S. W., Bayliss, M., et al. 2017, *ApJ*, **843**, 28
- Meneghetti, M., Cui, W., Rasia, E., et al. 2023, *A&A*, **678**, L2
- Meneghetti, M., Davoli, G., Bergamini, P., et al. 2020, *Sci*, **369**, 1347
- Meneghetti, M., Natarajan, P., Coe, D., et al. 2017, *MNRAS*, **472**, 3177
- Meneghetti, M., Ragagnin, A., Borgani, S., et al. 2022, *A&A*, **668**, A188
- Munari, E., Grillo, C., De Lucia, G., et al. 2016, *ApJL*, **827**, L5
- Napier, K., Sharon, K., Dahle, H., et al. 2023, *ApJ*, **959**, 134
- Natarajan, P., Chadayammuri, U., Jauzac, M., et al. 2017, *MNRAS*, **468**, 1962
- Navarro, J. F., Frenk, C. S., & White, S. D. M. 1996, *ApJ*, **462**, 563
- Oemler, A., Clardy, K., Kelson, D., Walth, G., & Villanueva, E., 2017 COSMOS: Carnegie Observatories System for MultiObject Spectroscopy, Astrophysics Source Code Library, ascl:1705.001
- Ofek, E. O., 2014 MAAT: MATLAB Astronomy and Astrophysics Toolbox, Astrophysics Source Code Library, ascl:1407.005
- Oke, J. B. 1974, *ApJS*, **27**, 21
- Patel, N. R., Jauzac, M., Niemiec, A., et al. 2024, *MNRAS*, **533**, 4500
- Patrício, V., Richard, J., Carton, D., et al. 2018, *MNRAS*, **477**, 18
- Postman, M., Coe, D., Benitez, N., et al. 2012, *ApJS*, **199**, 25
- Rajan, A. 2010, WFC3 Data Handbook, Version 2.0 (Baltimore, MD: STScI)
- Remolina González, J. D. 2021, PhD thesis, Univ. Michigan doi:10.7302/2889
- Richard, J., Kneib, J.-P., Ebeling, H., et al. 2011, *MNRAS*, **414**, L31
- Rigby, J. R., Vieira, J. D., Phadke, K. A., et al. 2025, *ApJ*, **978**, 108
- Rivera-Thorsen, T. E., Dahle, H., Chisholm, J., et al. 2019, *Sci*, **366**, 738
- Robertson, A. 2021, *MNRAS*, **504**, L7
- Robertson, A., Harvey, D., Massey, R., et al. 2019, *MNRAS*, **488**, 3646
- Ruel, J., Bazin, G., Bayliss, M., et al. 2014, *ApJ*, **792**, 45
- Salmon, B., Coe, D., Bradley, L., et al. 2020, *ApJ*, **889**, 189
- Schrabback, T., Bocquet, S., Sommer, M., et al. 2021, *MNRAS*, **505**, 3923
- Sharon, K., Bayliss, M. B., Dahle, H., et al. 2020, *ApJS*, **247**, 12
- Simcoe, R. A., Burgasser, A. J., Schechter, P. L., et al. 2013, *PASP*, **125**, 270
- Sirks, E. L., Oman, K. A., Robertson, A., Massey, R., & Frenk, C. 2022, *MNRAS*, **511**, 5927
- Smith, G. P., Kneib, J.-P., Smail, I., et al. 2005, *MNRAS*, **359**, 417
- Somboonpanyakul, T., McDonald, M., Gaspari, M., Stalder, B., & Stark, A. A. 2021, *ApJ*, **910**, 60
- Stalder, B., Stark, A. A., Amato, S. M., et al. 2014, *Proc. SPIE*, **9147**, 91473Y
- Stark, D. P., Auger, M., Belokurov, V., et al. 2013, *MNRAS*, **436**, 1040
- Tam, S.-I., Umetsu, K., & Amara, A. 2022, *ApJ*, **925**, 145
- Tokayer, Y. M., Dutra, I., Natarajan, P., et al. 2024, *ApJ*, **970**, 143
- Vanderlinde, K., Crawford, T. M., de Haan, T., et al. 2010, *ApJ*, **722**, 1180
- Welch, B., Coe, D., Zackrisson, E., et al. 2022, *ApJL*, **940**, L1
- Windhorst, R. A., Cohen, S. H., Jansen, R. A., et al. 2023, *AJ*, **165**, 13
- Zitrin, A., Seitz, S., Monna, A., et al. 2017, *ApJL*, **839**, L11